This manuscript is a non-peer reviewed Earth ArXiv preprint and has been submitted to EPSL.

Compressibility of ferropericlase at high-temperature: evidence for the iron spin crossover in seismic tomography

Viktoria E. Trautner[a], Stephen Stackhouse[b], Alice R. Turner[a], Paula Koelemeijer[a,c], D. Rhodri Davies[d], Alba San José Méndez[e], Niccolo Satta[a], Alexander Kurnosov[f], Hanns-Peter Liermann[e], Hauke Marquardt[a]

[a]Department of Earth Sciences, University of Oxford, OX1 3AN Oxford, United Kingdom; [b]School of Earth and Environment, University of Leeds, LS2 9JT Leeds, United Kingdom; [c]Department of Earth Sciences, Royal Holloway University of London, TW20 0EX Egham, United Kingdom; [d]The Research School of Earth Sciences, Australian National University, ACT 2600 Canberra, Australia; [e]Deutsches Elektronen-Synchrotron (DESY), 22607 Hamburg, Germany; [f]Bayerisches Geoinstitut BGI, University of Bayreuth, 95440 Bayreuth, Germany;

Corresponding author: Viktoria Trautner (viktoria.trautner@earth.ox.ac.uk)

Highlights:

- First measurements of the elastic softening in ferropericlase at high temperature
- New theoretical calculations of the iron spin crossover benchmarked by experiments
- Signature in seismic tomography investigated using synthetic tomography models
- Synthetic models with a realistic resolution are compared to data-based models
- Evidence for the presence of mixed-spin ferropericlase in Earth's lower mantle

Abstract

The iron spin crossover in ferropericlase, the second most abundant mineral in Earth's lower mantle, causes changes in a range of physical properties, including seismic wave velocities. Understanding the effect of temperature on the spin crossover is essential to detect its signature in seismic observations and constrain its occurrence in the mantle. Here, we report the first experimental results on the spin crossover-induced bulk modulus softening at high temperatures, derived directly from time-resolved x-ray diffraction measurements during continuous compression of $(Mg_{0.8}Fe_{0.2})O$ in a resistive-heated dynamic diamond-anvil cell. We present new theoretical calculations of the spin crossover at mantle temperatures benchmarked by the experiments. Based on our results, we create synthetic seismic tomography models to investigate the signature of the spin crossover in global seismic tomography. A tomographic filter is applied to allow for meaningful comparisons between the synthetic models and data-based seismic tomography models, like SP12RTS. A negative anomaly in the correlation between V_s variations and V_c variations (S-C correlation) is found to be the most suitable measure to detect the presence of the spin crossover in tomographic models. When including the effects of the spin crossover, the misfit between the synthetic model and SP12RTS is reduced by 63%, providing strong evidence for the presence of the spin crossover, and hence ferropericlase, in the lower mantle. Future improvement of seismic resolution may facilitate a detailed mapping of spin state using the S-C correlation, providing constraints on mantle temperatures, thanks to the temperature sensitivity of the spin crossover.

1. Introduction

$(Mg_{1-x}Fe_x)O$ ferropericlase is the second most abundant mineral in a pyrolitic lower mantle, constituting approximately 18 % by volume (Irifune et al., 2010). Under pressures relevant to the lower mantle, the iron atoms in ferropericlase gradually undergo a spin-pairing transition from high-spin (HS) to low-spin (LS) state, where d-electrons are redistributed over atomic orbitals (Badro et al., 2003). As a result, the ionic radius of iron is reduced and the unit-cell volume of ferropericlase decreases, causing an anomalous softening of the bulk modulus across the spin crossover (Crowhurst et al., 2008; Fei, Zhang, et al., 2007; Lin et al., 2005; Marquardt et al., 2009; Marquardt et al., 2018; Solomatova et al., 2016; Wentzcovitch et al., 2009; Wu et al., 2013; Yang et al., 2015). The spin crossover-induced bulk modulus softening has been reported to cause major changes in a wide range of properties of ferropericlase, that are relevant for large-scale geophysical processes (Lin et al., 2013). Therefore, detecting the signature of the spin crossover in seismic observations and constraining its occurrence and distribution in the lower mantle is of vital importance to improve geodynamic models and constrain chemical heterogeneity in the mantle. In an ideal case, it would be possible to construct three-dimensional (3D) maps of lateral and vertical variations in the spin state of ferropericlase based on seismic tomography.

The enhanced compressibility of ferropericlase in the mixed-spin (MS) region causes a drop in P-wave (V_P) and bulk sound velocities (V_C), while no substantial effect of the spin crossover on the shear modulus (G) and S-wave velocities (V_S) has been reported (Marquardt et al., 2009; Murakami et al., 2012; Wu et al., 2013; Yang et al., 2015). Consequently, a high ratio of V_S to V_P and negative correlation between V_S and V_C are seen as characteristic features of the spin crossover, that might allow for its detection in seismic observations (Marquardt et al., 2009). However, the depth, broadness and shape of the iron spin crossover are not yet well-constrained at temperatures of the lower mantle, hampering a robust detection by seismic methods. Previous experimental studies at high temperature did not measure the bulk modulus of ferropericlase directly, but had to rely on assumptions about its behaviour across the spin crossover (Mao et al., 2011) or have been limited to low iron contents and pressures below the onset of the spin crossover (Yang et al., 2016). While theoretical calculations generally predict that the spin crossover broadens and shifts to higher pressures with increasing temperature (Holmström & Stixrude, 2015; Sun et al., 2022; Tsuchiya et al., 2006; Wentzcovitch et al., 2009; Wu et al., 2013), a verification of different computational predictions has been hampered by the absence of an experimental benchmark. Calculated spin state phase diagrams show major differences depending on the assumptions made, leading to significant uncertainties in any attempt to detect the spin crossover signature in seismic observables (e.g. Sun et al., 2022).

Nevertheless, first efforts to identify the spin crossover signal in seismological models have been reported (Cammarano et al., 2010; Kennett, 2021; Shephard et al., 2021). In particular, recent work by Shephard et al. (2021) takes advantage of the differing effects of the spin crossover on P- and S-wave velocities, suggesting that the spin crossover might be detectable in cold parts of the lower mantle. However, in addition to the current mineral physics uncertainties, the seismic tomography models investigated in the previous work lack internal consistency and realistic seismic resolution has not been accounted for.

Here, we present the first direct experimental determination of the bulk modulus softening of ferropericlase across the spin crossover at high temperature. We further present a new theoretical model that reproduces our high-temperature experimental results, as well as previous measurements at room temperature, allowing us to robustly predict the signature of the spin crossover at relevant mantle temperatures. We use these experimentally-verified computations to convert the 3D temperature variations predicted by a geodynamic model to high-resolution maps of seismic velocity variations in the deep mantle. By applying a tomographic filter, we are able to directly compare the results from our synthetic tomography model to tomographic model SP12RTS, a joint P- and S-wave model. We demonstrate that the fit between the synthetic model and SP12RTS is improved when the effects of the spin crossover in ferropericlase are included, illustrating the impact of our new mineral physics data. Our study thus provides strong indications that the spin crossover in ferropericlase is present in the Earth's mantle and that lateral and vertical variations in spin state may be investigated using seismic tomography models.

2. Methods

2.1 Experimental approach

Powder of $(Mg_{0.8}Fe_{0.2})O$ was synthesized from stoichiometric mixtures of reagent grade MgO and Fe_2O_3, treated in a gas-mixing furnace at 1250°C at an oxygen fugacity 2 log units below the fayalite-magnetite-quartz (FMQ) buffer (Marquardt & Miyagi, 2015). Platinum powder was mixed with the sample as pressure marker and this mixture was loaded without a pressure transmitting medium in two diamond-anvil cells (DACs), RH1 and RH2, with 150 µm culet size diamonds. Rhenium gaskets with inserts of $Fe_{0.79}Si_{0.06}B_{0.15}$ metallic glass were used to avoid parasitic Re peaks (Dong et al., 2022). A resistive-heated dynamic DAC (rh-dDAC) setup, that was developed at beamline P02.2 at PETRAIII, DESY, Germany (Méndez et al., 2020) was employed to continuously compress ferropericlase across the spin crossover pressure range. During compression, time-resolved X-ray diffraction measurements were conducted, which allowed us to collect quasi-continuous volume-pressure data. The compression experiments were performed at the ECB using monochromatic synchrotron x-ray radiation with a fixed wavelength of 0.4836 Å. A fast GaAs 2.3 LAMBDA detector (Pennicard et al., 2018) was employed to collect diffraction images with single image exposure times of 200 ms, capturing about 20% of the Debye-Scherrer diffraction rings.

Two types of experiments were conducted in the rh-dDAC (see Supporting Information SI fig. S1): (1) Continuous compression along a pre-programmed pressure ramp, and (2) pressure cycling over a limited pressure interval (Marquardt et al., 2018). In cell RH1, a total of three ramp experiments were measured at ~900 K. Single diffraction images were collected every ~50 K during heating to target temperature and the sample was cooled down to room temperature between ramps. During heating before the third ramp, 3.5 sinusoidal pressure oscillations of 0.2 Hz were applied to the sample every ~50 K. The amplitude of the cycling is related to the voltage applied to the piezo-actuator and the tightness of the cell and varies from 1-3 GPa (SI table S1). A single compression ramp was measured at ~1100 K in cell RH2. The cell was then cooled down to room temperature and heated again to 1450 K, while pressure cycling measurements with amplitudes of 1-19 GPa were conducted every ~50 K. Maximum compression rates during ramp experiments ranged from 0.17 GPa/s to 0.3 GPa/s and pressure increased by 16-34 GPa in each ramp, together covering pressures between 33 GPa and 105 GPa (SI table S1). Temperature measurements before and after each run from two type-R thermocouples mounted close to the tips of the diamonds were used to estimate temperature variations during the experimental run, which were less than 3%.

The program Dioptas (Prescher & Prakapenka, 2015) was used to integrate and background-correct diffraction images. A Python code for batch-processing of time-resolved diffraction data (Wang, B., 2022) was used on the integrated data to extract the peak positions of ferropericlase and platinum. The average unit-cell volume of platinum from the $(111)_{Pt}$, $(200)_{Pt}$ and $(220)_{Pt}$ reflections, weighted by the uncertainty of the peak-fit, was used to derive pressure, employing previously published third-order Birch-Murnaghan equation of state (EoS) parameters (Fei, Ricolleau, et al., 2007). Similarly, the unit-cell volume of ferropericlase was derived from the weighted average of the $(111)_{Fp}$, $(200)_{Fp}$ and $(220)_{Fp}$ reflections. Line-shift analysis of the utilized reflections (Shim et al., 2000; Singh & Takemura, 2001) showed that the differential stresses present during the ramp experiment measured in cell RH2 at 1100 K were high compared to the other experiments (SI section S1.1 and fig. S2). We found that the volumes derived from the $(111)_{Fp}$ and $(220)_{Fp}$ reflections are closest to the volumes measured during the pressure oscillation experiments at the same temperature and under lower stress conditions. Therefore, we chose to use the weighted average of the volumes from the $(111)_{Fp}$ and $(220)_{Fp}$ reflections only for the ramp at 1100 K. Uncertainties in pressure and unit-cell volume of ferropericlase were estimated from the difference between diffraction lines.

The smooth nature and high pressure-resolution of the compression ramps permits direct calculation of the isothermal bulk modulus (K_T) by numerical differentiation, according to its thermodynamic definition: $K_T = -V \cdot \left.\frac{\partial P}{\partial V}\right)_T$ (Méndez et al., 2021). K_T is calculated from the slope of a linear fit to measured volumes V as a function of pressure, i.e. $V(P)$, that fall in a chosen pressure interval around the target pressure. The error in K_T is propagated from the uncertainty in V and the standard error of the slope of the linear fit. When choosing the pressure interval, there is a trade-off between the uncertainties in the derived bulk moduli and the effective pressure resolution (Méndez et al., 2022). An interval of 5 GPa was found to be the best compromise for the ramps measured in RH1, while a 10 GPa interval was used for the ramp measured in RH2. Following Marquardt et al. (2018), the $V(P)$ data collected during pressure cycling at seismic frequencies was used to calculate the bulk modulus at each temperature step (SI section 1.2). The quality of the diffraction images collected during pressure cycling in RH2 was not sufficient to extract a reliable bulk modulus value from the $V(P)$ data.

2.2 Ab-initio calculations

Two types of calculations were performed. Lattice dynamics calculations were performed to determine the difference in the static and vibrational free energy of ferropericlase in different spin states, allowing calculation of the spin crossover. Molecular dynamics were performed to determine the elastic properties of ferropericlase in a fixed high or low-spin state. Both sets of results were combined to estimate the properties of ferropericlase through the spin crossover. For all calculations we used the Vienna Ab-initio Simulation Package (VASP) (Kresse & Furthmüller, 1996a, b) employing the projector augmented wave method (Blöchl, 1994; Kresse & Joubert, 1999), within the framework of density functional theory (DFT). The local density approximation (LDA) (Perdew & Zunger, 1981) was used for the exchange-correlation functional. The valence electron configurations for the potentials were $2p^6 3s^2$ for Mg, $3p^6 3d^7 4s^1$ for Fe, and $2s^2 2p^4$ for O. The cut-off for the plane-wave basis set was set to 600 eV.

In order to describe the correlated *d* electrons of iron in ferropericlase, we utilized the LDA+U scheme of Dudarev et al. (1998), in which only the difference between onsite Coulomb interaction parameter U and onsite exchange parameter J is meaningful. In the present work, we used U - J = 3.3 eV, which was found to lead to the best agreement with experimental values for the spin crossover pressure in ferropericlase at 300 K (Méndez et al., 2022), and is similar to the 3.0 eV used in other studies of the spin crossover (Muir & Brodholt, 2015). Since the LDA is known to underestimate pressure, we calculated a correction using the method outlined by Oganov et al. (2001), including the thermal pressure term calculated from our lattice dynamics calculations. The correction was calculated to be +3.5 GPa, based on the ambient condition volume of 76.1A^3 reported by Speziale et al. (2007). This correction is applied to our high-temperature results (both lattice dynamics and molecular dynamics).

2.2.1 Approach to spin transition calculations

In their pioneering work, Tsuchiya et al. (2006) and Wentzcovitch et al. (2009) calculated the fraction of LS iron in ferropericlase from an expression similar to:

$$n(P,T) = \frac{1}{1+m(2S+1)\left(\frac{\Delta G_{HS-LS}(P,T)}{k_B X_{Fe} T}\right)}, \tag{1}$$

where m is the electronic configuration degeneracy (m = 3 for HS and m = 1 for LS), S is the spin quantum number (S = 2 for HS and S= 0 for LS), $\Delta G_{HS-LS}(P,T)$ is the difference between the static and vibrational components of the Gibbs free energy of the high- and low-spin states, X_{Fe} is the fraction of iron, and k_B is the Boltzmann constant. This derivation assumes ideal mixing of high- and low-spin ions. We will refer to this approach as the single spin transition method (SSTM), since it only involves calculation of $\Delta G_{HS-LS}(P,T)$ for a single transition (from full HS to full LS). This method tends to lead to a spin crossover that is narrower at ambient-temperature than experimental results (Méndez et al., 2022).

Later work by Holmström and Stixrude (2015) demonstrated that favourable enthalpy of mixing of high- and low-spin ions leads to a broader spin crossover in better agreement with experiment. Further studies have proposed alternative methods, which include a non-ideal mixing model, with and without the contribution of magnetic entropy (Sun et al., 2022). Building on this, we recently showed that good agreement is obtained with ambient-temperature experimental results if, rather than assuming ideal mixing of high- and low-spin states, one calculates the series of successive spin transitions between stable spin states, from high- to low-spin (Méndez et al., 2022). In this method Equation 1 is applied to each individual spin transition, $\Delta G_{HS-LS}(P,T)$ is the difference between the static and vibrational components of the Gibbs free energy of the higher and lower spin states, X_{Fe} the fraction of iron weighted by the fraction of iron involved in the spin transition, and k_B is the Boltzmann constant. The overall *n* value for a model is then a weighted average of the *n* values for the individual spin transitions, where the weights are the fraction of iron atoms in the model involved in the successive spin transitions. We will refer to this approach as the multiple spin transition method (MSTM), as it requires the calculation of $\Delta G_{HS-LS}(P,T)$ for multiple spin transitions.

Preliminary calculations showed that difference in the results of the SSTM and MSTM are only significant at low temperature (<1000 K), where it is possible for a spin transition in one particular iron atom to finish before on in another iron atom begins. At lower mantle temperatures, both methods lead to similar results (SI figs. S5-S7), since all iron atoms are undergoing a spin transition and so the order of the spin transitions is irrelevant. Here, we chose to use the MSTM to compare with experimental results between 300 K and 1450 K.

2.2.2 Spin state calculations

Prior to performing lattice dynamics calculations, we investigated the effect of model size and arrangement of iron atoms on the spin crossover (SI sections S2-S3 and figs. S3-S6). Based on the results, we selected a 216-atom ferropericlase model (Configuration 10) with a $(Mg_{0.8148}Fe_{0.1852})O$

composition (i.e. 20 iron atoms in the model) for our production calculations. This model is larger than those in our previous work (Méndez et al., 2022), allowing on-axis iron atom neighbour pairs, while avoiding infinite repeating sequences of Fe and O atoms, arising from finite-size effects associated with the use of periodic boundary conditions. The latter was shown to have a non-negligible effect on the calculated spin crossover (Méndez et al., 2022). In accordance with the observations of Waychunas et al. (1994), the positions of the iron atoms were chosen at random. The coordinates of the iron atoms in all models studied in this work are listed in SI tables S2 and S3.

Since it was not feasible to calculate the vibrational free energy for all possible spin states for a 216-atom model, in the first instance, we calculated the stable mixed-spin states between the high- and low-spin states at 0K, neglecting the vibrational free energy contribution, and used those to compute the fraction of LS iron (SI sections S3-S5). Lattice dynamics calculations were then performed to calculate the vibrational free energy for only the stable mixed-spin states at 0 K (SI table S4).

For comparison, a small number of spin transition calculations were also performed using a hybrid functional, comprising the LDA with a 0.25 fraction of exact exchange. These showed good agreement with our LDA+U calculations at 300 K, with some small differences along a mantle geotherm below 1500 km (SI section S5 and fig. S8).

2.2.3 Elastic constants of ferropericlase

Molecular dynamics simulations were used to calculate the elastic properties, as opposed to lattice dynamics calculations, for two reasons: molecular dynamics simulations account for all anharmonic effects, which may become important at lower mantle temperatures; and the large cell used in the lattice dynamics calculations made calculating elastic constants using lattice dynamics prohibitively computationally expensive.

Preliminary calculations showed that the elastic properties of ferropericlase are less sensitive to magnetic state and arrangement of iron than the spin crossover, permitting the use of a smaller 64-

atom model for molecular dynamics simulations (SI section S6). The model used has a $(Mg_{0.8125}Fe_{0.1875})O$ composition (i.e. 6 iron atoms in the model) and an arrangement of iron atoms identical to the symmetric model used in our previous work (Méndez et al., 2022). High-temperature elastic constants were calculated for ferropericlase, fixed in a HS and LS state, from molecular dynamics simulations (NVT ensemble) using the Nosé thermostat to maintain constant temperature (Nosé, 1984), see SI section S7 for details. Isothermal and adiabatic elastic properties were calculated at 4 pressures and 6 temperatures. These are shown in SI figure S9 and listed in tables S5 and S6. Comparison of isothermal bulk moduli from our lattice dynamics calculations with those from our molecular dynamics simulations show good agreement (SI section S8 and fig. S10).

To predict elastic constants at other pressures and temperatures a weighted linear least-squares fit was made to values at the same temperature to determine values at the desired temperature and then values at the two nearest pressures points were used to interpolate or extrapolate to the desired pressure (SI fig. S11). To predict densities at other pressures and temperatures a weighted linear least-squares fit was made to values at the same temperature, to determine four values at the desired temperature, and these were then fit using a second-order Birch-Murnaghan equation of state (Birch, 1947; Murnaghan, 1944). To calculate the elastic constants of ferropericlase through the spin crossover we used the equations derived by Wu et al. (2013) (SI section S9).

2.3 Synthetic tomography models

To understand the effect of the iron spin crossover in ferropericlase on global seismic tomography, specifically its effect on the relationships between seismic velocities in such models, we constructed synthetic seismic tomography models from which we can calculate the ratio between V_S and V_P variations (here-after denoted as S/P ratio) and the correlation between V_S and V_C variations (here-after denoted as S-C correlation). We follow the methodology employed by Koelemeijer et al. (2018) with some adaptations as described below.

Rather than assuming a random distribution of temperatures in the mantle, we use the predicted present-day temperature distribution in the mantle based on a high-resolution isochemical mantle circulation model (Davies et al., 2012; see Koelemeijer et al., 2018 for more details). To convert these temperature variations to seismic velocities, we employ a thermodynamic database that describes the elastic parameters for any combination of pressure and temperature in the mantle for a given bulk mantle composition. However, existing databases based on thermodynamic mineralogical models (e.g. Stixrude & Lithgow-Bertelloni, 2011; Stixrude & Lithgow-Bertelloni, 2022) include ferropericlase only in the HS state.

To obtain the required thermodynamic database for ferropericlase in different spin states, we first linearly interpolate our experimentally-verified computations for density and bulk modulus obtained at a few fixed temperatures (300, 1000, 2000, 3000 and 4000 K) to a spacing of 50 K, before linearly interpolating to every 1 GPa in pressure. We then calculate Voigt-Reuss-Hill average properties for a mantle of pyrolitic composition in a simplified six-component system using the thermodynamic database of Stixrude and Lithgow-Bertelloni (2011, personal communication 2019), but replacing the phase properties of ferropericlase with our results for the MS phase. The phase properties for HS ferropericlase in the published model of Stixrude and Lithgow-Bertelloni (2011) match with our new computational results for HS ferropericlase with relative differences of less than 0.5 % along the geotherm (SI fig. S12). In addition, incorporating our results for HS ferropericlase does not change the relationships between seismic velocities.

We convert the temperatures in the mantle circulation model to seismic velocities using the adapted thermodynamic database, including either our own HS or MS ferropericlase results. The resulting high-resolution seismic mantle models describe realistic mantle structures, that we can use to calculate the relationships between seismic velocities in order to investigate the expected effect of the spin crossover in ferropericlase in the Earth's mantle. Specifically, we calculate the S-C correlation, as well as the S/P ratio. In both cases, we directly use the spherical harmonic coefficients that describe the tomography models after reparameterization, using the same approach as in Koelemeijer et al. (2018). We focus on the radially averaged values of these quantities, in order to remove any geographic dependence due to the plate reconstruction model used in the geodynamic simulation.

We cannot directly compare the high-resolution synthetic models to data-derived tomography models from the literature, because these represent a filtered and weaker version of actual mantle structures. To enable a meaningful comparison, we multiply our high-resolution synthetic models with the resolution matrix of model SP12RTS (Koelemeijer et al., 2016). This is one of few existing tomography models that inverted jointly for V_S and V_P variations in the mantle without imposing an a-priori scaling, which is crucial for studying the relationships between different seismic velocities. It also provides the associated resolution matrix (or tomographic filter), which allows us to capture the heterogeneous data coverage and inherent damping of the tomographic inversion. Therefore, we can perform like-to-like and quantitative comparisons between our synthetic tomography models with HS or MS ferropericlase and SP12RTS itself. By calculating the relationships between seismic velocities in both the high-resolution seismic models and the filtered models, we can determine the theoretically expected effect of the spin crossover in the Earth's mantle as well as what we may observe realistically at present in an existing tomography model.

3. Results and discussion

3.1 Comparison of experimental and computational results on the anomalous compressibility of ferropericlase at high temperature

The experimental unit-cell volumes of $(Mg_{0.8}Fe_{0.2})O$ collected at various temperatures up to 1450 K are shown in fig. 1a as a function of pressure, together with previous data collected at 300 K (Méndez et al., 2022) and the isotherms from our ab-initio calculations. At approximately 50 GPa, there is a clear drop in the volumes determined from the compression ramps measured at 900 K. This change in the trend of the V-P curve is attributed to the onset of the spin crossover. Our experimental data agree well with the new theoretical predictions at most pressures and temperatures. The only previously published data on ferropericlase at high temperature (Komabayashi et al., 2010; Mao et al., 2011) were collected in laser-heated DACs and diverge from our experimental and computational results at pressures above ~40 GPa (SI fig. S13), which may be due to the use of a different pressure standard, an inhomogeneous temperature distribution or chemical segregation that might occur during laser-heating (Sinmyo & Hirose, 2010).

We derived the isothermal bulk modulus directly from the slope of our V(P) data, without having to fit an equation of state or rely on model assumptions (see also Méndez et al., 2021; Méndez et al., 2022), providing the first experimental constraints on the bulk modulus softening of ferropericlase at high temperature. In fig. 1b, the experimentally determined bulk moduli are plotted as a function of pressure, together with our computational predictions and results from previous studies. Our experimental and theoretical results at 900 K agree well overall; both show a broad and asymmetric spin crossover-induced softening of the bulk modulus between around 45 GPa and 105 GPa. Pressure cycling measurements performed at selected *P-T* conditions confirm the softening of the bulk modulus at seismic frequencies (SI fig. S14). There is good agreement between our results and Brillouin spectroscopy measurements at 900 K of the bulk modulus of $(Mg_{0.92}Fe_{0.08})O$ by Yang et al. (2016), although those measurements are limited to pressures below the spin crossover and made on ferropericlase with lower iron content. The ab initio calculations performed here also fit well with previous results from dDAC experiments at room temperature (Méndez et al., 2022).

In our new computations a random distribution of iron atoms in the crystal lattice is accounted for and rather than assuming ideal mixing of HS and LS states, the enthalpy of mixed spin states is calculated, in addition to full HS and LS states (see Méndez et al., 2022 for details). This is in contrast to older studies based on models assuming an ideal mixing of HS and LS iron and a uniform arrangement of iron atoms (Wentzcovitch et al., 2009; Wu et al., 2013). Comparison of our calculated bulk moduli with those of Wu et al. (2013) show excellent agreement in regions where ferropericlase is in a pure high- or low-spin state, but differences emerge for the mixed-spin state (SI fig. S15). Similar observations are observed for the shear moduli (SI fig. S16), except for some slight difference at higher pressure and temperature. This suggests that differences arise mainly from different values for the low-spin fraction of iron. Wu et al. (2013) predict a sharper bulk modulus softening over a narrower depth range and a larger amplitude than observed in our experimental results (fig. 1b). More recent studies have taken into account a favourable enthalpy of mixing of HS and LS states (Holmström & Stixrude, 2015; Sun et al., 2022), but these predict a wider spin crossover than found in this work.

The agreement between our high-temperature experimental results and our computations at high temperature confirm the robustness of the later, allowing us to confidently extend the theoretical model to mantle temperatures. Our theoretical results for density (ρ) and seismic velocities (V_S, V_P and V_C) along several isotherms are shown in fig. 2a-d for $(Mg_{0.8125}Fe_{0.1875})O$. Along a typical geotherm, the onset of the spin crossover is predicted to occur around 1500 km depth, while full low-spin state is never reached (SI fig. S17), indicating that spin crossover-induced changes to the physical properties of ferropericlase are expected to affect most of the lower mantle (see also Méndez et al., 2022). We find a substantial reduction in V_P and V_C across the spin crossover, while V_S and ρ are barely affected and increase continuously (fig. 2a-d).

3.2 Signature of the spin crossover in seismic tomography

To understand how the signature of the spin crossover in ferropericlase will show up in data-based tomography models, we constructed synthetic seismic tomography models with and without the spin crossover, using the methodology described in section 2.3. Specifically, we combine the present-day temperature field of a high-resolution mantle circulation model (Davies et al., 2012; for details see Koelemeijer et al., 2018) with the temperature dependence of the spin crossover from our experimentally benchmarked calculations to create maps of the spin state and seismic velocity variations in the lower mantle (fig. 3). The distribution of heterogeneity in the mantle circulation model is, to first order, consistent with seismologically imaged distribution, as it is largely dictated by 300 Myr of prescribed surface plate velocities. The resulting ring of downwellings around the Pacific and upwelling return flow in the Pacific and under Africa cause temperature variations in the lower mantle (fig. 3 top row). These temperature variations lead to substantial lateral variations in spin fractions.

In the bottom two rows of figure 3, bulk sound velocity variations are shown at different depths in the lower mantle for models with HS-only and MS ferropericlase. Our results clearly show that at depths where the elastic behaviour of ferropericlase is influenced by the spin crossover, bulk sound velocity variations are much less pronounced in the MS model compared to the HS model, indicating an insensitivity to temperature. In some regions, we even observe a positive correlation between temperature and bulk sound velocity, i.e. relative velocity variations are low in colder areas (e.g. 1490 km depth) and high in hotter areas (e.g. 2122 km depth). This inversion of the temperature dependence can be explained by the shift of the bulk modulus softening in ferropericlase to higher pressures with increasing temperature, which leads to a positive temperature dependence of V_C (= $\sqrt{\frac{K}{\rho}}$) at specific *P*-*T* conditions (fig. 1b and 2d), as previously suggested by Marquardt et al. (2009); Wu (2016).

The seismic signature of the spin crossover becomes more evident when looking at the radially-averaged correlation between V_S and V_C variations in depth profiles of the synthetic tomographic models (fig. 4a). The anti-correlated temperature dependence of shear and bulk sound velocity in the spin crossover depth range leads to a strong negative anomaly in the S-C correlation with a maximum around 1800 km depth, which is absent in the HS model. A second minimum in the S-C correlation at lowermost mantle depths is the result of the bridgmanite to post-perovskite transition (Koelemeijer et al., 2018), which was included in the construction of the models.

To allow for a direct comparison between our high-resolution synthetic velocity models and data-derived seismic tomography models with a limited tomographic resolution, we apply a tomographic filter (see section 2.3). After filtering, the spin crossover signal in the depth profile of the mixed-spin synthetic tomography model becomes less pronounced, with a more smeared out and weakened negative S-C correlation (fig. 4b). Nonetheless, differences between the HS and MS models remain clearly visible. The MS model shows a lower S-C correlation between 1200 km and 2300 km depth than the HS model, indicating that the S-C correlation can serve as a distinguishing feature in seismic observations for the detection of the iron spin crossover, even if a realistic limited seismic resolution is accounted for.

A high V_S / V_P ratio has also been suggested in the past as a characteristic signature of the spin crossover (Marquardt et al., 2009). While we observe a modest increase in the ratio of V_S variations to V_P variations at mid-lower mantle depths in the high-resolution MS model as a result of the spin crossover (SI fig. S18), the differences between the HS and MS models largely disappear after tomographic filtering. This suggests that the S/P ratio is a less suitable measure for the detection of the spin crossover when accounting for the resolution achieved in current tomographic models.

When comparing our filtered synthetic tomography models to joint S- and P-wave model SP12RTS (Koelemeijer et al., 2016), we find that the negative S-C correlation at mid-lower mantle depths in SP12RTS is best reproduced by the synthetic model with ferropericlase in mixed-spin state (fig. 4b). Inclusion of the spin crossover significantly affects the L2 misfit with model SP12RTS between 1000 and 2500 km depth, reducing this on average by 63%, from 0.27 (HS) to 0.10 (MS) (fig. 4c). Given there is no other known process that has the same effect on seismic velocities at these mid mantle depths, these results strongly suggest that the negative S-C correlation in the mid-lower mantle is caused by the iron spin crossover in ferropericlase. Our work thus provides the first evidence for the visibility of the iron spin crossover in ferropericlase in seismic tomography models while taking realistic tomographic resolution into account. This finding implies the presence of about 20% of ferropericlase throughout the lower mantle, supporting recent works in favour of a pyrolitic lower mantle composition (Kurnosov et al., 2017; Wang, X. et al., 2015; Zhang et al., 2016), as opposed to a perovskitic average composition (Murakami et al., 2012). If the depth resolution in seismic tomography models describing V_C variations improve in the future, a more detailed mapping of the spin crossover might become feasible and could ultimately allow for pinpointing average mantle temperature at mid-mantle depths, as well as lateral temperature variations from comparisons between synthetic and data-derived tomographic models.

Our theoretical computations, that are used for the construction of the seismic tomography models are for a single composition of ferropericlase, i.e. an iron content of 18.75 at. %. Although this is close to the composition expected for the majority of the lower mantle (Irifune et al., 2010; Murakami, 2005), it has been suggested that the iron partitioning between ferropericlase and bridgmanite is affected by the spin crossover, leading to an increase of iron content of ferropericlase (Lin et al., 2013). In addition, ferropericlase may be enriched in iron in the lowermost mantle and the low seismic velocities in Ultra Low-Velocity Zones ULVZs have been attributed to the presence of iron-rich ferropericlase (Wicks et al., 2010; Wicks et al., 2017). The spin crossover-induced bulk modulus softening is expected to shift to higher pressures with increasing iron content (Solomatova et al., 2016), so compositional variations in lower mantle-ferropericlase would affect the spin state, in addition to temperature variations. Such mechanisms should be considered in future studies to further resolve the spin state of the lower mantle and its effect on mantle physical properties.

4. Conclusions

First experimental results on the spin crossover-induced elastic softening in ferropericlase at high temperature are reproduced by a new theoretical model that takes the position of iron atoms in the crystal lattice into account. By combining the experimentally-verified computations with the present-day temperature distribution in the mantle predicted by geodynamics, we constructed high-resolution synthetic seismic tomography models. The theoretically expected seismic signature of the spin crossover in the lower mantle is expressed as a strong negative anomaly in the S-C correlation and a moderately increased S/P ratio. After applying a tomographic filter to account for a realistic tomographic resolution of data-driven tomography models, we find that a negative S-C correlation is the most suitable measure for detection of the spin crossover in seismic observations. Including the spin crossover in the filtered synthetic model improves the fit in the S-C correlation with global tomography model SP12RTS between 1000 and 2500 km depth by 63%. Our findings provide the first evidence for the visibility of the spin crossover in seismic tomography models when realistic tomographic resolution is accounted for and hence indicate the presence of mixed-spin ferropericlase in large parts of the lower mantle. Improvement of seismic resolution will facilitate a detailed mapping of the spin crossover using the S-C correlation. In the future, this may be translated to 3D maps of temperature and iron distribution in the mid-lower mantle, by reversing the protocol employed in this study.

Acknowledgments

This research received funding through the European Union's Horizon 2020 research and innovation Programme (ERC grant DEEP-MAPS, ID: 864877 awarded to HM), as well as from NERC (grant number NE/K006290/1 awarded to SS) and from Royal Society grants awarded to PK (RGF\EA\181029 and URF\R1\180377). The authors acknowledge DESY (Hamburg, Germany), a member of the Helmholtz Association HGF, for the provision of experimental facilities. The calculations were performed on ARC3 and ARC4, part of the High-Performance Computing facilities at the University of Leeds, United Kingdom. PK would like to thank Carolina Lithgow-Bertelloni and Lars Stixrude for providing the thermodynamic database used for converting the temperature distribution to seismic velocities.

Conflict of interest

The authors declare no conflicts of interest relevant to this study.

References

Badro, J., Fiquet, G., Guyot, F., Rueff, J.-P., Struzhkin, V. V., Vankó, G. & Monaco, G. (2003). Iron Partitioning in Earth's Mantle: Toward a Deep Lower Mantle Discontinuity. *Science*, *300*(5620), 789-791. https://doi.org/10.1126/science.1081311

Birch, F. (1947). Finite elastic strain of cubic crystals. *Physical review*, *71*(11), 809-824. https://doi.org/10.1103/PhysRev.71.809

Blöchl, P. E. (1994). Projector augmented-wave method. *Physical Review B*, *50*(24), 17953-17979. https://doi.org/10.1103/PhysRevB.50.17953

Cammarano, F., Marquardt, H., Speziale, S. & Tackley, P. J. (2010). Role of iron-spin transition in ferropericlase on seismic interpretation: A broad thermochemical transition in the mid mantle? *Geophysical Research Letters*, *37*(3), L03308. https://doi.org/10.1029/2009gl041583

Crowhurst, J. C., Brown, J. M., Goncharov, A. F. & Jacobsen, S. D. (2008). Elasticity of (Mg,Fe)O Through the Spin Transition of Iron in the Lower Mantle. *Science*, *319*(5862), 451-453. https://doi.org/10.1126/science.1149606

Davies, D. R., Goes, S., Davies, J. H., Schuberth, B. S. A., Bunge, H. P. & Ritsema, J. (2012). Reconciling dynamic and seismic models of Earth's lower mantle: The dominant role of thermal heterogeneity. *Earth and Planetary Science Letters*, *353-354*(253-269. https://doi.org/10.1016/j.epsl.2012.08.016

Dong, W., Glazyrin, K., Khandarkhaeva, S., Fedotenko, T., Bednarčík, J., Greenberg, E., et al. (2022). Fe0.79Si0.07B0.14 metallic glass gaskets for high-pressure research beyond 1 Mbar. *Journal of Synchrotron Radiation*, *29*(5), 1167-1179. https://doi.org/10.1107/s1600577522007573

Dudarev, S. L., Botton, G. A., Savrasov, S. Y., Humphreys, C. J. & Sutton, A. P. (1998). Electron-energy-loss spectra and the structural stability of nickel oxide: An LSDA+U study. *Physical Review B*, *57*(3), 1505-1509. https://doi.org/10.1103/PhysRevB.57.1505

Fei, Y., Ricolleau, A., Frank, M., Mibe, K., Shen, G. & Prakapenka, V. (2007). Toward an internally consistent pressure scale. *Proc Natl Acad Sci U S A*, *104*(22), 9182-9186. https://doi.org/10.1073/pnas.0609013104

Fei, Y., Zhang, L., Corgne, A., Watson, H., Ricolleau, A., Meng, Y. & Prakapenka, V. (2007). Spin transition and equations of state of (Mg, Fe)O solid solutions. *Geophysical Research Letters*, *34*(17), L17307. https://doi.org/10.1029/2007gl030712

Holmström, E. & Stixrude, L. (2015). Spin crossover in ferropericlase from first-principles molecular dynamics. *Phys Rev Lett*, *114*(11), 117202. https://doi.org/10.1103/PhysRevLett.114.117202

Irifune, T., Shinmei, T., McCammon, C. A., Miyajima, N., Rubie, D. C. & Frost, D. J. (2010). Iron Partitioning and Density Changes of Pyrolite in Earth's Lower Mantle. *Science*, *327*(5962), 193-195. https://doi.org/10.1126/science.1181443

Kennett, B. L. N. (2021). The relative behaviour of bulk and shear modulus as an indicator of the iron spin transition in the lower mantle. *Earth and Planetary Science Letters*, *559*(https://doi.org/10.1016/j.epsl.2021.116808

Koelemeijer, P., Ritsema, J., Deuss, A. & Van Heijst, H.-J. (2016). SP12RTS: a degree-12 model of shear- and compressional-wave velocity for Earth's mantle. *Geophysical Journal International*, *204*(2), 1024-1039. https://doi.org/10.1093/gji/ggv481

Koelemeijer, P., Schuberth, B. S. A., Davies, D. R., Deuss, A. & Ritsema, J. (2018). Constraints on the presence of post-perovskite in Earth's lowermost mantle from tomographic-geodynamic model comparisons. *Earth and Planetary Science Letters*, *494*(226-238. https://doi.org/10.1016/j.epsl.2018.04.056

Komabayashi, T., Hirose, K., Nagaya, Y., Sugimura, E. & Ohishi, Y. (2010). High-temperature compression of ferropericlase and the effect of temperature on iron spin transition. *Earth and Planetary Science Letters*, *297*(3-4), 691-699. https://doi.org/10.1016/j.epsl.2010.07.025

Kresse, G. & Furthmüller, J. (1996a). Efficient iterative schemes for ab initio total-energy calculations using a plane-wave basis set. *Physical Review B*, *54*(16), 11169-11186. https://doi.org/10.1103/PhysRevB.54.11169

Kresse, G. & Furthmüller, J. (1996b). Efficiency of ab-initio total energy calculations for metals and semiconductors using a plane-wave basis set. *Computational Materials Science*, *6*(1), 15-50. https://doi.org/https://doi.org/10.1016/0927-0256(96)00008-0

Kresse, G. & Joubert, D. (1999). From ultrasoft pseudopotentials to the projector augmented-wave method. *Physical Review B*, *59*(3), 1758-1775. https://doi.org/10.1103/PhysRevB.59.1758

Kurnosov, A., Marquardt, H., Frost, D. J., Ballaran, T. B. & Ziberna, L. (2017). Evidence for a Fe3+-rich pyrolitic lower mantle from (Al,Fe)-bearing bridgmanite elasticity data. *Nature*, *543*(7646), 543-546. https://doi.org/10.1038/nature21390

Lin, J.-F., Struzhkin, V. V., Jacobsen, S. D., Hu, M. Y., Chow, P., Kung, J., et al. (2005). Spin transition of iron in magnesiowüstite in the Earth's lower mantle. *Nature*, *436*(7049), 377-380. https://doi.org/10.1038/nature03825

Lin, J.-F., Speziale, S., Mao, Z. & Marquardt, H. (2013). Effects of the Electronic Spin Transitions of Iron in Lower Mantle Minerals: Implications for Deep Mantle Geophysics and Geochemistry. *Reviews of Geophysics*, *51*(2), 244-275. https://doi.org/10.1002/rog.20010

Mao, Z., Lin, J.-F., Liu, J. & Prakapenka, V. B. (2011). Thermal equation of state of lower-mantle ferropericlase across the spin crossover. *Geophysical Research Letters*, *38*(23), L23308. https://doi.org/10.1029/2011gl049915

Marquardt, H., Speziale, S., Reichmann, H. J., Frost, D. J. & Schilling, F. R. (2009). Single-crystal elasticity of (Mg0.9Fe0.1)O to 81 GPa. *Earth and Planetary Science Letters*, *287*(3-4), 345-352. https://doi.org/10.1016/j.epsl.2009.08.017

Marquardt, H. & Miyagi, L. (2015). Slab stagnation in the shallow lower mantle linked to an increase in mantle viscosity. *Nature Geoscience*, *8*(4), 311-314. https://doi.org/10.1038/ngeo2393

Marquardt, H., Buchen, J., Mendez, A. S. J., Kurnosov, A., Wendt, M., Rothkirch, A., et al. (2018). Elastic Softening of (Mg0.8Fe0.2)O Ferropericlase Across the Iron Spin Crossover Measured at Seismic Frequencies. *Geophysical Research Letters*, *45*(14), 6862-6868. https://doi.org/10.1029/2018gl077982

Méndez, A. S. J., Marquardt, H., Husband, R. J., Schwark, I., Mainberger, J., Glazyrin, K., et al. (2020). A resistively-heated dynamic diamond anvil cell (RHdDAC) for fast compression x-ray diffraction experiments at high temperatures. *Rev Sci Instrum*, *91*(7), 073906. https://doi.org/10.1063/5.0007557

Méndez, A. S. J., Trybel, F., Husband, R. J., Steinle-Neumann, G., Liermann, H.-P. & Marquardt, H. (2021). Bulk modulus of H2O across the ice VII–ice X transition measured by time-resolved x-ray diffraction in dynamic diamond anvil cell experiments. *Physical Review B*, *103*(6), 064104. https://doi.org/10.1103/physrevb.103.064104

Méndez, A. S. J., Stackhouse, S., Trautner, V., Wang, B., Satta, N., Kurnosov, A., et al. (2022). Broad elastic softening of (Mg,Fe)O ferropericlase across the iron spin crossover and a mixed-spin lower mantle. *Journal of Geophysical Research: Solid Earth*, https://doi.org/10.1029/2021jb023832

Muir, J. M. R. & Brodholt, J. P. (2015). Elastic properties of ferropericlase at lower mantle conditions and its relevance to ULVZs. *Earth and Planetary Science Letters*, *417*(40-48. https://doi.org/10.1016/j.epsl.2015.02.023

Murakami, M. (2005). Post-perovskite phase transition and mineral chemistry in the pyrolitic lowermost mantle. *Geophysical Research Letters*, *32*(3), https://doi.org/10.1029/2004gl021956

Murakami, M., Ohishi, Y., Hirao, N. & Hirose, K. (2012). A perovskitic lower mantle inferred from high-pressure, high-temperature sound velocity data. *Nature*, *485*(7396), 90-94. https://doi.org/10.1038/nature11004

Murnaghan, F. D. (1944). The Compressibility of Media under Extreme Pressures. *Proceedings of the National Academy of Sciences*, *30*(9), 244-247. https://doi.org/10.1073/pnas.30.9.244

Nosé, S. (1984). A unified formulation of the constant temperature molecular dynamics methods. *The Journal of Chemical Physics*, *81*(1), 511-519. https://doi.org/10.1063/1.447334

Oganov, A. R., Brodholt, J. P. & Price, G. D. (2001). Ab initio elasticity and thermal equation of state of MgSiO3 perovskite. *Earth and Planetary Science Letters*, *184*(3), 555-560. https://doi.org/https://doi.org/10.1016/S0012-821X(00)00363-0

Pennicard, D., Smoljanin, S., Pithan, F., Sarajlic, M., Rothkirch, A., Yu, Y., et al. (2018). LAMBDA 2M GaAs—A multi-megapixel hard X-ray detector for synchrotrons. *Journal of instrumentation*, *13*(1), C01026-C01026. https://doi.org/10.1088/1748-0221/13/01/C01026

Perdew, J. P. & Zunger, A. (1981). Self-interaction correction to density-functional approximations for many-electron systems. *Physical Review B*, *23*(10), 5048.

Prescher, C. & Prakapenka, V. B. (2015). DIOPTAS: a program for reduction of two-dimensional X-ray diffraction data and data exploration. *High Pressure Research*, *35*(3), 223-230. https://doi.org/10.1080/08957959.2015.1059835

Shephard, G. E., Houser, C., Hernlund, J. W., Valencia-Cardona, J. J., Trønnes, R. G. & Wentzcovitch, R. M. (2021). Seismological expression of the iron spin crossover in ferropericlase in the Earth’s lower mantle. *Nature Communications*, *12*(1), https://doi.org/10.1038/s41467-021-26115-z

Shim, S.-H., Duffy, T. S. & Shen, G. (2000). The stability and P-V-T equation of state of CaSiO3perovskite in the Earth's lower mantle. *Journal of Geophysical Research: Solid Earth*, *105*(B11), 25955-25968. https://doi.org/10.1029/2000jb900183

Singh, A. K. & Takemura, K. (2001). Measurement and analysis of nonhydrostatic lattice strain component in niobium to 145 GPa under various fluid pressure-transmitting media. *Journal of Applied Physics*, *90*(7), 3269-3275. https://doi.org/10.1063/1.1397283

Sinmyo, R. & Hirose, K. (2010). The Soret diffusion in laser-heated diamond-anvil cell. *Physics of the Earth and Planetary Interiors*, *180*(3-4), 172-178. https://doi.org/10.1016/j.pepi.2009.10.011

Solomatova, N. V., Jackson, J. M., Sturhahn, W., Wicks, J. K., Zhao, J., Toellner, T. S., et al. (2016). Equation of state and spin crossover of (Mg,Fe)O at high pressure, with implications for explaining topographic relief at the core-mantle boundary. *American Mineralogist*, *101*(5), 1084-1093. https://doi.org/10.2138/am-2016-5510

Speziale, S., Lee, V. E., Clark, S. M., Lin, J. F., Pasternak, M. P. & Jeanloz, R. (2007). Effects of Fe spin transition on the elasticity of (Mg,Fe)O magnesiowüstite and implications for the seismological properties of the Earth's lower mantle. *Journal of Geophysical Research*, *112*(

Stixrude, L. & Lithgow-Bertelloni, C. (2011). Thermodynamics of mantle minerals - II. Phase equilibria. *Geophysical Journal International*, *184*(3), 1180-1213. https://doi.org/10.1111/j.1365-246x.2010.04890.x

Stixrude, L. & Lithgow-Bertelloni, C. (2022). Thermal expansivity, heat capacity and bulk modulus of the mantle. *Geophysical Journal International*, *228*(2), 1119-1149.

Sun, Y., Zhuang, J. & Wentzcovitch, R. M. (2022). Thermodynamics of spin crossover in ferropericlase: an improved LDA+Usc calculation. *Electronic Structure*, *4*(014008. https://doi.org/10.1088/2516-1075/ac522b

Tsuchiya, T., Wentzcovitch, R. M., Da Silva, C. R. S. & De Gironcoli, S. (2006). Spin Transition in Magnesiowüstite in Earth’s Lower Mantle. *Physical Review Letters*, *96*(19), https://doi.org/10.1103/physrevlett.96.198501

Wang, B. (2022). Batch Peaks Fitting Script in Python for Time-Resolved XRD Data Analysis (v1.0.0) [Software]. Zenodo. https://doi.org/10.5281/zenodo.7457445

Wang, X., Tsuchiya, T. & Hase, A. (2015). Computational support for a pyrolitic lower mantle containing ferric iron. *Nature Geoscience*, *8*(7), 556-559. https://doi.org/10.1038/ngeo2458

Waychunas, G. A., Dollase, W. A. & Ross II, C. R. (1994). Short-range order measurements in MgO-FeO and MgO-LiFeO, solid solutions byDLS simulation-assisted EXAFS analysis. *American Mineralogist*, *79*(3-4), 274-288.

Wentzcovitch, R. M., Justo, J. F., Wu, Z., Da Silva, C. R. S., Yuen, D. A. & Kohlstedt, D. (2009). Anomalous compressibility of ferropericlase throughout the iron spin cross-over. *Proceedings of the National Academy of Sciences*, *106*(21), 8447-8452. https://doi.org/10.1073/pnas.0812150106

Wicks, J. K., Jackson, J. M. & Sturhahn, W. (2010). Very low sound velocities in iron-rich (Mg,Fe)O: Implications for the core-mantle boundary region. *Geophysical Research Letters*, *37*(15), L15304. https://doi.org/10.1029/2010gl043689

Wicks, J. K., Jackson, J. M., Sturhahn, W. & Zhang, D. (2017). Sound velocity and density of magnesiowüstites: Implications for ultralow-velocity zone topography. *Geophysical Research Letters*, *44*(5), 2148-2158. https://doi.org/10.1002/2016gl071225

Wu, Z., Justo, J. F. & Wentzcovitch, R. M. (2013). Elastic anomalies in a spin-crossover system: ferropericlase at lower mantle conditions. *Phys Rev Lett*, *110*(22), 228501. https://doi.org/10.1103/PhysRevLett.110.228501

Wu, Z. (2016). Velocity structure and composition of the lower mantle with spin crossover in ferropericlase. *Journal of Geophysical Research: Solid Earth*, *121*(4), 2304-2314. https://doi.org/10.1002/2015jb012667

Yang, J., Tong, X., Lin, J.-F., Okuchi, T. & Tomioka, N. (2015). Elasticity of Ferropericlase across the Spin Crossover in the Earth's Lower Mantle. *Scientific Reports*, *5*(1), 17188. https://doi.org/10.1038/srep17188

Yang, J., Lin, J. F., Jacobsen, S. D., Seymour, N. M., Tkachev, S. N. & Prakapenka, V. B. (2016). Elasticity of ferropericlase and seismic heterogeneity in the Earth's lower mantle. *Journal of Geophysical Research: Solid Earth*, *121*(12), 8488-8500. https://doi.org/10.1002/2016jb013352

Zhang, S., Cottaar, S., Liu, T., Stackhouse, S. & Militzer, B. (2016). High-pressure, temperature elasticity of Fe- and Al-bearing MgSiO3: Implications for the Earth's lower mantle. *Earth and Planetary Science Letters*, *434*(C), 264-273. https://doi.org/10.1016/j.epsl.2015.11.030

Figures

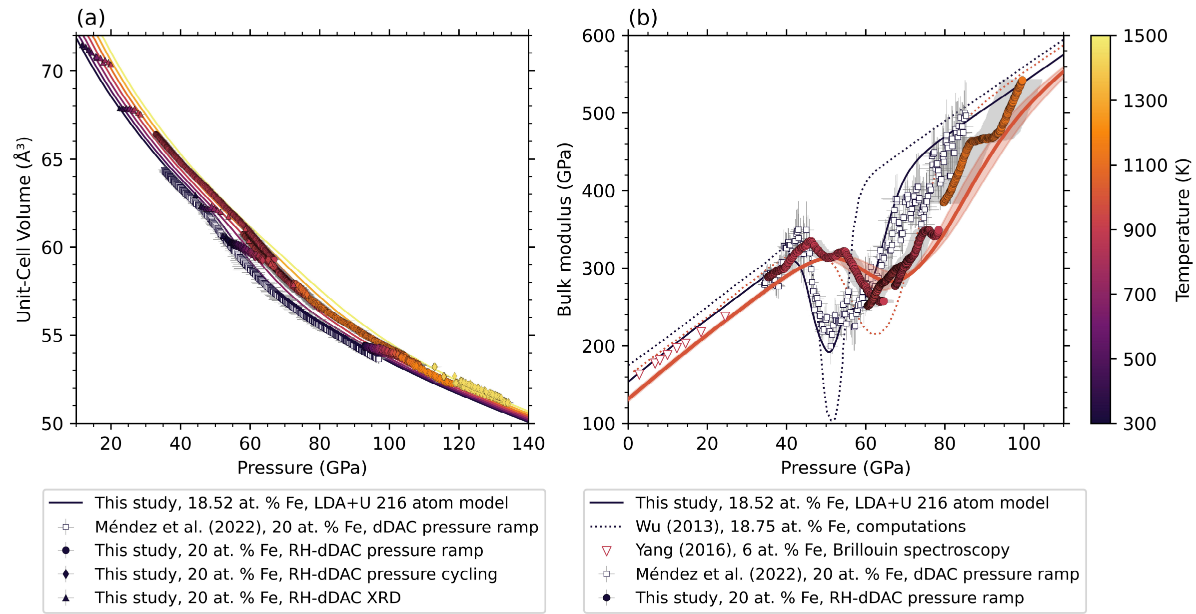

Figure 1 a) Volume-pressure (V-P) data collected during pressure ramp (filled circles) and pressure cycling (filled diamonds) experiments in the RH-dDAC at various temperatures, together with the predicted V-P curves along isotherms from our numerical calculations. Also shown are previous results of a pressure ramp experiment at room temperature (open squares, Méndez et al., 2022) and measurements taken while heating (filled triangles). b) Experimental bulk moduli as a function of pressure at high temperature, derived from pressure ramp experiments (filled circles). The grey shaded region indicates the pressure interval over which the V-P curve was differentiated to derive the bulk modulus. The 1000 ± 100 K isotherm from our lattice dynamics calculations is shown as a solid orange line with a shaded region and the 300 K isotherm is indicated by a solid dark line. Previous results from dDAC ramp experiments at room temperature are shown as open squares (Méndez et al., 2022). Also shown are Brillouin spectroscopy results at 900 K (open triangles, Yang et al., 2016), as well as previous computational results at 300 K and 1000 K (dotted lines, Wu et al., 2013). Note that the results from both Yang et al. (2016) and Wu et al. (2013) are for the adiabatic bulk modulus, whereas the results from this study and Méndez et al. (2022) are for the isothermal bulk modulus.

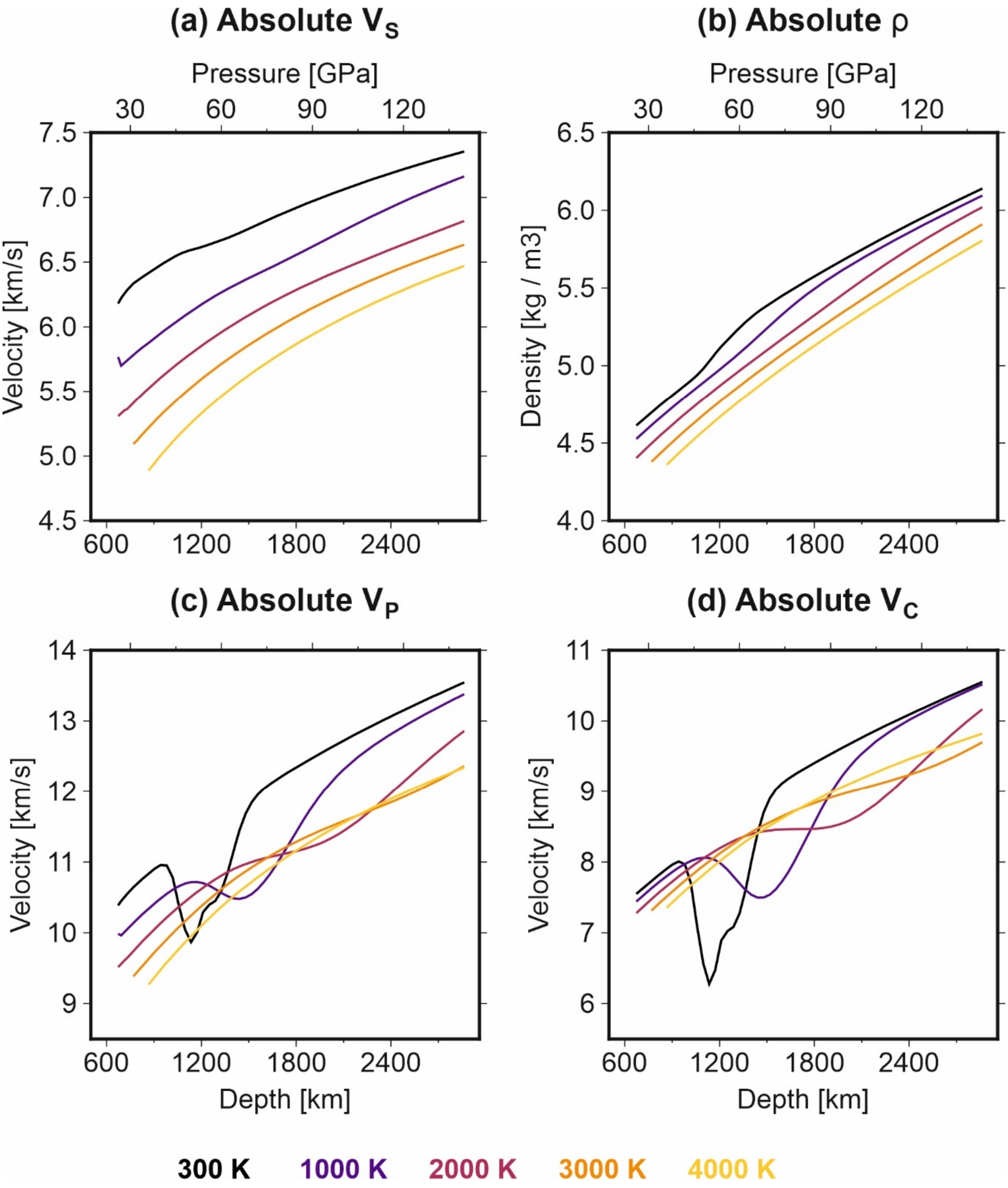

Figure 2 Theoretical predictions of absolute (a) S-wave velocity V_S, (b) density, (c) P-wave velocity V_P, and (d) bulk sound velocity V_C of ferropericlase as a function of depth in in Earth's mantle. The iron spin crossover leads to a marked reduction in V_P and V_C, while V_S and ρ increase continuously with depth with only slight changes in slope.

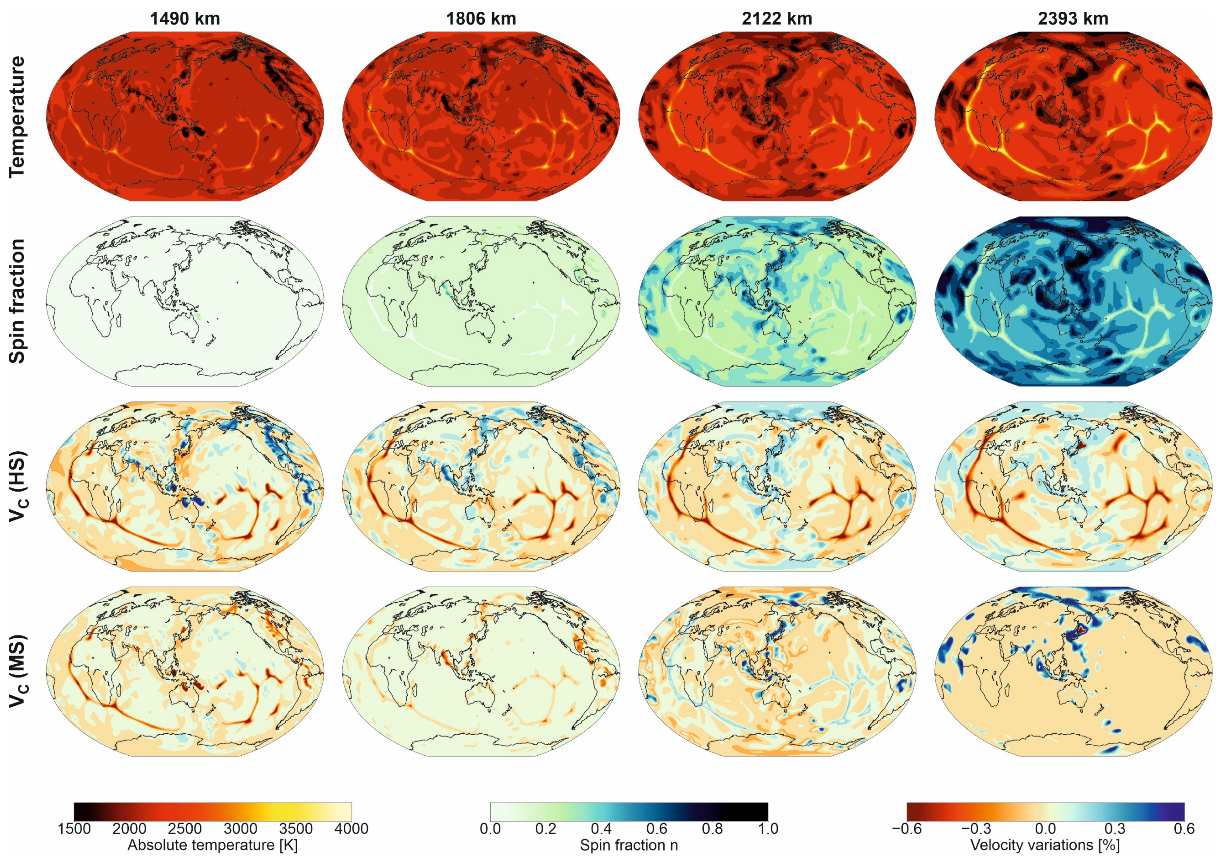

Figure 3 Maps of temperature, spin fraction and bulk sound velocity variations for high-spin HS and mixed-spin MS ferropericlase at different depths in the lower mantle in our synthetic models. The top row shows the temperature field generated from a high-resolution geodynamic model and the second row shows the fraction of LS ferropericlase corresponding to these temperatures, as predicted by ab- initio calculations. The last two rows show bulk sound velocity V_C variations when ferropericlase is assumed to stay in a high-spin state and when the effects of the iron spin crossover are included, respectively, in the high-resolution synthetic seismic tomography models.

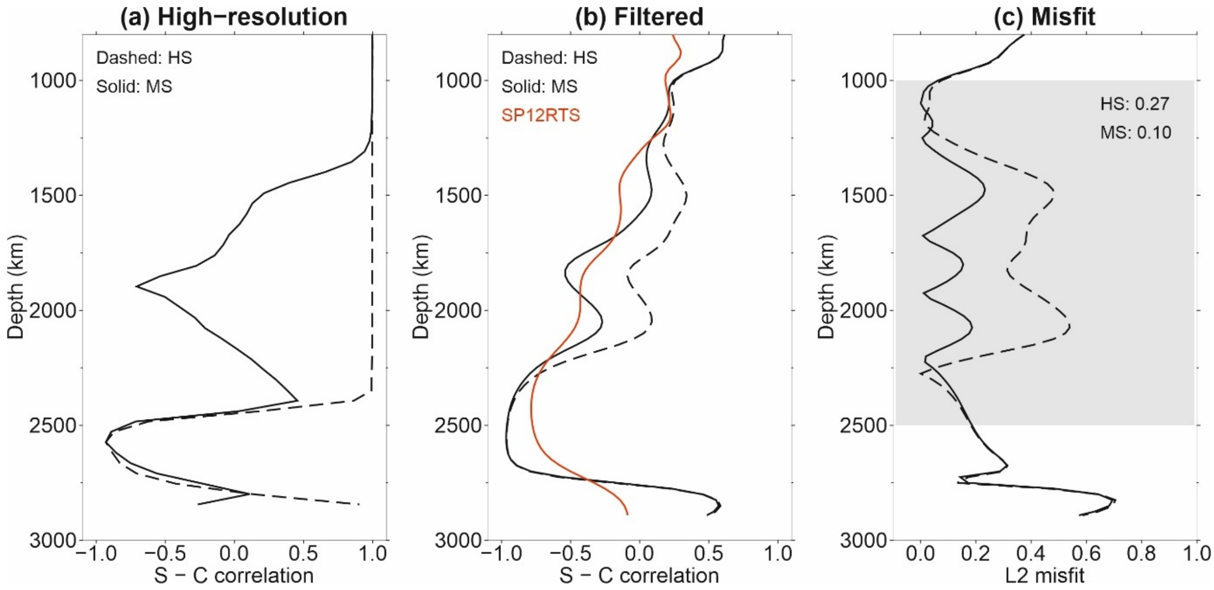

Figure 4 Prediction of radially averaged correlation between V_S and V_C variations (S – C correlation) along depth profiles in the synthetic tomography models with high-spin HS and mixed-spin MS ferropericlase (dashed and solid lines, respectively). (a) Results without the application of a tomographic filter, showing a strong negative anomaly in the mid lower mantle produced by the spin crossover. (b) Results of the synthetic models with tomography filtering compared to seismic tomography model SP12RTS (red) (Koelemeijer et al., 2016). (c) L2 misfit between the predicted S - C correlations of the HS and MS models and model SP12RTS itself. The average misfit between 1000 and 2500 km depth (grey shaded region) is reduced by 63% from 0.27 (HS) to 0.1 (MS) when the effects of the iron spin crossover in ferropericlase are included.

Supporting Information for

Compressibility of ferropericlase at high-temperature: evidence for the iron spin crossover in seismic tomography

Viktoria E. Trautner[a], Stephen Stackhouse[b], Alice R. Turner[a], Paula Koelemeijer[a,c], D. Rhodri Davies[d], Alba San José Méndez[e], Niccolo Satta[a], Alexander Kurnosov[f], Hanns-Peter Liermann[e], Hauke Marquardt[a]

[a]Department of Earth Sciences, University of Oxford, OX1 3AN Oxford, United Kingdom; [b]School of Earth and Environment, University of Leeds, LS2 9JT Leeds, United Kingdom; [c]Department of Earth Sciences, Royal Holloway University of London, TW20 0EX Egham, United Kingdom; [d]The Research School of Earth Sciences, Australian National University, ACT 2600 Canberra, Australia; [e]Deutsches Elektronen-Synchrotron (DESY), 22607 Hamburg, Germany; [f]Bayerisches Geoinstitut BGI, University of Bayreuth, 95440 Bayreuth, Germany;

Corresponding author: Viktoria Trautner (viktoria.trautner@earth.ox.ac.uk)

Contents of this file

Text S1. RH-dDAC experiments

S1.1 Line-width analysis

To evaluate the stress condition of our experiments we obtained the product of elastic anisotropy factor (S) and uniaxial stress component (t) from a line-shift analysis of the utilized reflections (Singh & Takemura, 2001). To calculate deviatoric stress in a sample, S of the material and its dependence on temperature and pressure must be well-constrained, which is currently not the case for platinum and $(Mg_{0.8}Fe_{0.2})O$ at our experimental conditions. Notwithstanding, the product St can be used as an indicator of the magnitude of uniaxial stress, with Shim et al. (2000) proposing a St value between -0.005 and 0.005 as a criterion for quasi-hydrostaticity. Most of our measurements yield St values between approximately -0.01 and 0.01 for both platinum and ferropericlase (fig. S2), exceeding the limit of $|St| \leq 0.005$. This indicates non-hydrostatic stresses of moderate magnitude were present during some of the measurements. The ramp measured in cell RH2 at 1100 K forms an exception, with St values of -0.016 in ferropericlase, indicating a high differential stress. Because the volumes derived from the $(111)_{Fp}$ and $(220)_{Fp}$ reflections are closest to the volumes measured during the pressure oscillation experiments at the same temperature with lower St values of around -0.006, we chose to use these reflections only for the ramp at 1100 K.

S1.2 Bulk modulus calculation from pressure cycling experiments

Pressure cycling experiments were conducted in cell RH1 at temperatures between 300 K and 900 K in steps of approximately 50 K (table S1). At each temperature step, 3.5 sinusoidal pressure oscillations were applied with a frequency of 0.2 Hz, while collecting diffraction images with an exposure time of 0.2 s. During each experiment, a total of 100 datapoints was measured, with the first 15 points collected before pressure cycling commenced. The interval over which pressure was cycled varied between experiments, depending on the voltage applied and the tightness of the cell, and ranged from 0.9 to 2.9 GPa (table S1). The collected V(P) data was used to calculate the bulk modulus of $(Mg_{0.8}Fe_{0.2})O$ at each temperature step. A linear regression was applied to the 100 datapoints collected at each temperature to derive the slope of the V(P) curve and the volume V at the average pressure, which were then used to calculate the bulk modulus according to its thermodynamic definition: $K_T = -V \cdot \left.\frac{\partial P}{\partial V}\right)_T$ (Méndez et al., 2021).

Text S2 Investigation of finite-size effects on the spin crossover

In our previous investigation, the arrangement of iron atoms in our models was shown to have a non-negligible effect on the onset and breadth of the spin crossover (Méndez et al. 2022). This is a particular issue for 64-atom models for which finite-size effects, resulting from the use of periodic boundary conditions, can lead to an infinite repeating sequence of Fe and O atoms. Before proceeding to perform lattice dynamics calculations we therefore carried out preliminary calculations to examine how model size and the arrangement of iron influence the spin crossover. For these calculations we only calculated the 0 K spin transition pressure, i.e. the pressure, at 0 K, at which the enthalpy of the high- and low-spin states are equal. This was done by calculating the enthalpy difference at 20 GPa, 40 GPa, 60 GPa and 80 GPa.

The spin transition pressure was calculated for twenty 64-atom ferropericlase models, with a $Mg_{0.8125}Fe_{0.1875}$ composition, corresponding to 6 Fe atoms in a cell. These were identical to those described in our previous study (Méndez et al. 2022). In addition, we constructed ten new 216-atom models with a $(Mg_{0.8148}Fe_{0.1852})O$ composition, corresponding to 20 Fe atoms in a cell, as well as five 512-atom models with a $(Mg_{0.8125}Fe_{0.1875})O$ composition, corresponding to 48 Fe atoms in a cell. The larger 216-atom and 512-atom models allow iron on-axis neighbour pairs, while avoiding infinite repeating sequences of Fe and O atoms, arising from finite-size effects associated with the use of periodic boundary conditions.

Waychunas et al. (1994) showed that ferropericlase samples quenched from high-temperature exhibit random iron ordering. The arrangement of iron in the 64-atom models was chosen at random (Méndez et al. 2022). This was also the case for our 216-atom and 512-atom models, with the exception that arrangements of iron that contained an infinite repeating sequence of Fe and O atoms were rejected. The initial atomic coordinates of the iron atoms in our 216-atom and 512-atom models are listed in Tables S2 and S3.

For the iron concentrations investigated in this study, ferropericlase is paramagnetic above 300 K (Kantor et al., 2009; Lyubutin et al., 2013; Speziale et al., 2005). Initial high-spin states were approximated as a disordered collinear paramagnet i.e. iron atoms were randomly assigned either a spin up or spin down magnetic moment, under the constraint that the model had an overall net magnetic moment of zero. For comparison, calculations were also carried out on all models using ferromagnetic ordering.

For the 64-atoms models the Brillouin zone was sampled using a 2×2×2 Monkhorst-Pack grid (Monkhorst & Pack, 1976), while for the larger 216-atom and 512-atom models it was restricted to the gamma-point. These settings ensured that enthalpy differences were converged to within less than 1meV/atom. Other calculation parameters were identical those in the main text.

Since the LDA is known to underestimate pressure, we applied a pressure correction of +6 GPa calculated in previous work (Méndez et al. 2022). This correction is larger than the one applied to the results in the main text, as it also corrects for the thermal pressure, missing in 0 K calculations.

Our tests show that for the larger models, the range of spin transition pressures obtained for different arrangements of iron is narrower (fig. S3). In particular, for our 64-atom models the calculated spin transition pressures ranges from 40GPa to 48GPa, depending on the arrangement of iron, while for the 216-atom models the range is from 43GPa to 47GPa and for the 512-atom models the range is from 44GPa to 47GPa. This reduction in range is likely due to either the reduction of finite-size effects in the larger models, or the fact that a larger number of local iron environments are sampled within a model. In view of this, and the minor difference in the results for the 216-atom and 512-atom models, it was decided to use 216-atom models in this study. Configurations 1, 4 and 10 were chosen for further investigation, representing the upper limit, intermediate and lower limit of spin transition pressures (fig. S3).

Text S3 Investigation of iron arrangement

To examine the effect of iron arrangement on low-spin fraction at high-temperature, we computed it for three configurations, using the single spin transition method (SSTM) and the multiple spin transition method (MSTM), but neglecting the vibrational free energy (i.e. replacing $\Delta G_{HS-LS}(P)$ with $\Delta H_{HS-LS}(P)$ in Equation 1). The computational expense of lattice dynamics calculations makes studying multiple iron arrangements unfeasible for the MSTM. Neglecting vibrational free energy should make only a minor difference on the absolute low-spin fraction at 300K, but will be significant at lower mantle temperatures.

S3.1 Calculation of isothermal bulk modulus through the spin crossover

From the fraction of low-spin iron, calculated through the SSTM or MSTM, it is possible to calculate the isothermal bulk modulus. To do this one first needs the P-V equation of state of ferropericlase in the high- and low-spin states. Following the method of (Tsuchiya et al., 2006; Wentzcovitch et al., 2009), first the volume of ferropericlase through the spin crossover is determined, assuming ideal mixing pure low-spin and high-spin states

$$V(n) = (1-n)V_{HS} + nV_{LS} \tag{S2}$$

where $V(n)$ is the volume of ferropericlase with a low-spin fraction n, and V_{HS} and V_{LS} are the volumes of ferropericlase in the pure high- and low-spin states. The bulk modulus of ferropericlase in a mixed-spin state $K(n)$ is then determined from the following

$$\frac{V(n)}{K(n)} = (1-n)\frac{V_{HS}}{K_{HS}} + n\frac{V_{LS}}{K_{LS}} - (V_{LS} - V_{HS})\frac{\partial n}{\partial P} \tag{S3}$$

where K_{HS} and K_{LS} are the isothermal bulk moduli for the pure high- and low-spin states.

S3.2 Onset and breadth of the spin crossover at 300 K

The fraction of low-spin iron at 300K was calculated for the 216-atom models labelled Configuration 1, Configuration 4 and Configuration 10, using both SSTM and MSTM. For this, $\Delta H_{HS-LS}(P)$ was calculated at 20GPa, 40GPa, 60GPa, and 80GPa and the results fit to a second-order polynomial. In addition, the 0K volumes of the pure high- and low-spin states were calculated at 12 pressures between -10GPa and 140GPa. The pressure-volume data were fit to a third-order Birch-Murnaghan equation-of-state (Birch, 1947; Murnaghan, 1944), which were used to determine the volume of the pure high- and low-spin states (V_{HS}, V_{LS}) and corresponding bulk moduli (K_{HS}, K_{LS}), needed for Equations (S2) and (S3). Note that, in the calculations of bulk moduli we use 0K volumes to approximate 300K volumes. The difference is expected to be small and, in part, compensated by the pressure correction applied.

Our results (figs. S4 and S5) show that, even using 216-atom models, the arrangement of iron produces differences in the onset pressure of the spin crossover. In addition, the calculation method influences the breadth of the spin crossover. The SSTM produces a sharp crossover, whereas the MSTM produces a broader spin crossover, which is in better agreement with experimental results (Méndez et al. 2022). Looking at the calculated bulk moduli, using the MSTM (fig. S5), there is general agreement between the different configurations. Configuration 1 best matches the experimental onset pressure of the spin crossover, with those produced by Configuration 4 and 10 being a few GPa lower. However, Configuration 1 exhibits a pronounced second minimum at about 65GPa that is not observed in the experiments. Configuration 4 shows a steeper onset than that seen in the experiments. In view of this, and the expected increase in the spin transition pressure with the inclusion of vibrational free energy, Configuration 10 was chosen for our production calculations.

S3.3 Onset and breadth of the spin crossover along a mantle geotherm

Using the results from the calculation described above (Section S3.2) the fraction of low-spin iron was calculated along a typical mantle geotherm (Stixrude & Lithgow-Bertelloni, 2011). Note that, the calculations neglect vibrational free energy and so are inaccurate, but allow investigation of the effect of iron arrangement and calculation method.

Our results (fig. S6) show that, at the high temperatures in the lower mantle, the difference between the three arrangements of iron is small. In particular, the results for Configurations 4 and 10 are extremely similar, with the onset of spin crossover being slightly higher for Configuration 1, meaning that the fraction of low-spin iron is slightly lower at the base of the mantle. In addition, the difference between the results of the two calculations methods is small (fig. S6 and S7). This suggests that the SSTM used in previous works (Tsuchiya et al., 2006; Wentzcovitch et al., 2009; Wu et al., 2013) should give reasonable predictions of the low-spin fraction along a mantle geotherm, even if poor agreement is found with ambient-temperature experimental results.

Text S4 Lattice dynamics calculations details

For the lattice dynamics calculations, the model was optimized at 7 volumes between about 12-18 Å^3 per formula unit. Thermodynamic properties were calculated using PHON (Alfe, 2009) based on the finite displacement method, with displacements of ±0.02 Å. The Brillouin zone was sampled at the Γ-point. This ensured that all free-energy differences were converged to within less than 1 meV/atom. A third-order finite strain equation of state was fit to the calculated results.

The initial high-spin state was approximated as a disordered collinear paramagnet i.e. the iron atoms were randomly assigned either an initial spin up or spin down magnetic moment, under the constraint that the net magnetic moment was zero. Symmetry was switched off.

Text S5 Comparison of LDA+U calculations with those using a hybrid functional

The fixed value of U - J = 3.3eV used in our calculations was selected based on comparison with experimental data (Méndez et al. 2022). Previous investigations (Tsuchiya et al. 2006) using a self-consistent LDA+U method (Cococcioni & De Gironcoli, 2005) indicate that U changes slightly with pressure and is slightly different for high- and low-spin states. In order to validate our approach, we have performed some additional calculations using a hybrid functional comprising the LDA with a 0.25 fraction of exact exchange. Due to the large computational cost, calculations were only performed for Configuration 10 using the SSTM (and neglecting the vibrational free energy). Figure S8 shows there is general agreement between the results of LDA+U method and hybrid functional, with some small differences at the greatest depths along a mantle geotherm.

Text S6 Effects of magnetic state and iron arrangement on elastic properties

For molecular dynamics simulations, we used a 64-atom model with a $(Mg_{0.8125}Fe_{0.1875})O$ composition (i.e. 6 iron atoms in the model) and a symmetric arrangement of iron atoms (Méndez et al., 2022). Its symmetry reduced the number of strains required to calculate the elastic constants and thus, in turn, the number of computationally expensive molecular dynamics simulations. However, due to its smaller size, the model contains infinite repeating Fe-O-Fe-O sequences, arising from finite-size effects associated with the use of periodic boundary conditions. To validate using this arrangement of iron we calculated the 0 K elastic constants for it and twenty other arrangements of iron used in previous work (Méndez et al., 2022). Negligible difference was found in the calculated values of the bulk moduli, with a standard deviation less than 0.5% of the mean value. The standard deviation for the shear moduli was on the order of 1-2% of the mean value, with the shear modulus of the symmetric model being about 1-2% higher than the mean value. In addition to using a 64-atom model, due to difficulties in maintaining a high-spin disordered paramagnetic state at lower mantle pressures, our high-spin calculations used a ferromagnetic state. To justify using the ferromagnetic state, we calculated 0 K elastic constants at 20 GPa for both a ferromagnetic state and an antiferromagnetic state and found negligible difference.

Text S7 Molecular dynamics calculations details

For the calculation of high-temperature elastic constants for ferropericlase fixed in a high-spin and low-spin state, the simulation cell was first equilibrated at the desired temperature and pressure. The correct pressure was obtained by running multiple simulations and adjusting the lattice parameter. Elastic constants were calculated from linear stress-strain relations by applying one orthorhombic and one triclinic strain with magnitudes of ±1 % and ±2 %. Equilibrium simulations were run for 40 ps and simulations of the strained models were run for 20 ps. In all simulations the time-step was fixed at 1 fs. Errors in the time average of the stress tensors were computed taking into account correlation (Flyvbjerg & Petersen, 1989). Bulk and shear moduli were calculated as a Voigt-Reuss-Hill average.

Isothermal elastic constants were converted to corresponding adiabatic values via the method of Wallace (1972) as used in our earlier work (Stackhouse & Brodholt, 2007; Zhang et al., 2016). These calculations require additional thermodynamic parameters, e.g. the thermal stress tensor, which were calculated from further molecular dynamics simulation runs with the equilibrium lattice parameters, but with a temperature ±200 K of the equilibrium temperature.

For the calculation of elastic properties, using the 64-atom models, the Brillouin zone was sampled using a 2×2×2 Monkhorst-Pack grid (Monkhorst & Pack, 1976) for the 0 K elastic constant calculations and at the Γ-point for the high-temperature calculations. These setting ensured that the 0 K bulk and shear moduli were converged to within less than a percent and the high-temperature bulk and shear moduli were converged to within a few percent.

Text S8 Comparison of lattice dynamics and molecular dynamics calculations of K_T

In the present work, we have calculated the elastic properties of ferropericlase from molecular dynamics simulations, as shown in figure S9. The lattice dynamics calculations performed to calculate the fraction of low-spin iron, also allow calculation of the isothermal bulk modulus, using Equations S1, S2 and S3, but replacing $\Delta H_{HS-LS}(P)$ with $\Delta G_{HS-LS}(P,T)$ in S1. This was done for the 216-atom model labelled Configuration 10. The results are compared with the values for the isothermal bulk moduli calculated from the molecular dynamics simulations in figure S10. One can see that there is good agreement between the two sets of results. The molecular dynamics calculations were performed using a 64-atom simulation cell with a particular arrangement of iron atoms, while the lattice dynamics calculations were carried out using a 216-atom model with a different arrangement of iron atoms.

Text S9 Calculation of elastic constants through the spin crossover

To calculate the elastic constants of ferropericlase through the spin crossover we used the equations derived by Wu et al. (2013), where the compliances for the mixed-spin state are calculated from

$$S^{11}V = nS^{11}_{LS}V_{LS} + (1-n)nS^{11}_{HS}V_{HS} - \frac{1}{9}(V_{LS} - V_{HS})\frac{\partial n}{\partial P} \quad \text{(S4)}$$
$$S^{12}V = nS^{12}_{LS}V_{LS} + (1-n)nS^{12}_{HS}V_{HS} - \frac{1}{9}(V_{LS} - V_{HS})\frac{\partial n}{\partial P} \quad \text{(S5)}$$
$$S^{44}V = nS^{44}_{LS}V_{LS} + (1-n)nS^{44}_{HS}V_{HS} \quad \text{(S6)}$$

where the relationship between S^{ij} and C^{ij} for all spin states is

$$S^{11} = \frac{C_{11}+C_{12}}{C_{11}^2+C_{11}C_{12}-2C_{12}^2} \text{ and } C_{11} = \frac{S^{11}+S^{12}}{(S^{11})^2+S^{11}S^{12}-2(S^{12})^2} \quad \text{(S7)}$$
$$S^{12} = \frac{-C_{12}}{C_{11}^2+C_{11}C_{12}-2C_{12}^2} \text{ and } C_{12} = \frac{-S^{12}}{(S^{11})^2+S^{11}S^{12}-2(S^{12})^2} \quad \text{(S8)}$$
$$S^{44} = \frac{1}{C_{44}} \text{ and } C_{44} = \frac{1}{S^{44}} \quad \text{(S9)}$$

S^{ij}_{LS} and S^{ij}_{HS} are the compliances of the low-spin and high-spin states, C^{ij}_{LS} and C^{ij}_{HS} are the elastic constants for the low-spin and high-spin states, V_{HS} and V_{LS} are the volumes of the low-spin and high-spin states and $\frac{\partial n}{\partial P}$ is the pressure derivative of fraction of low-spin iron.

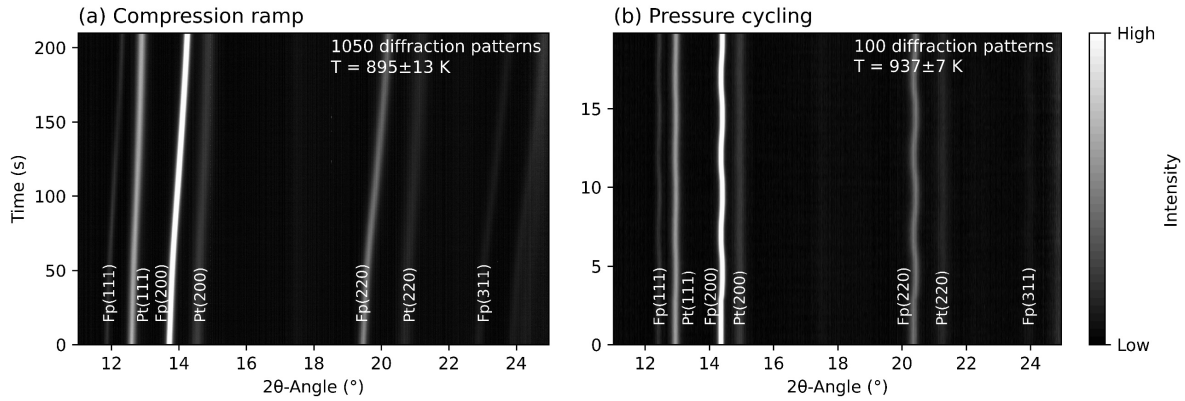

Figure S1. Representative contourplots consisting of stacked diffraction patterns of a) pressure ramp, and b) pressure oscillation experiments on $(Mg_{0.8}Fe_{0.2})O$ + platinum powders, measured in the RH-dDAC. Labels indicate the hkl indices of the diffraction peaks of ferropericlase (Fp) and platinum (Pt).

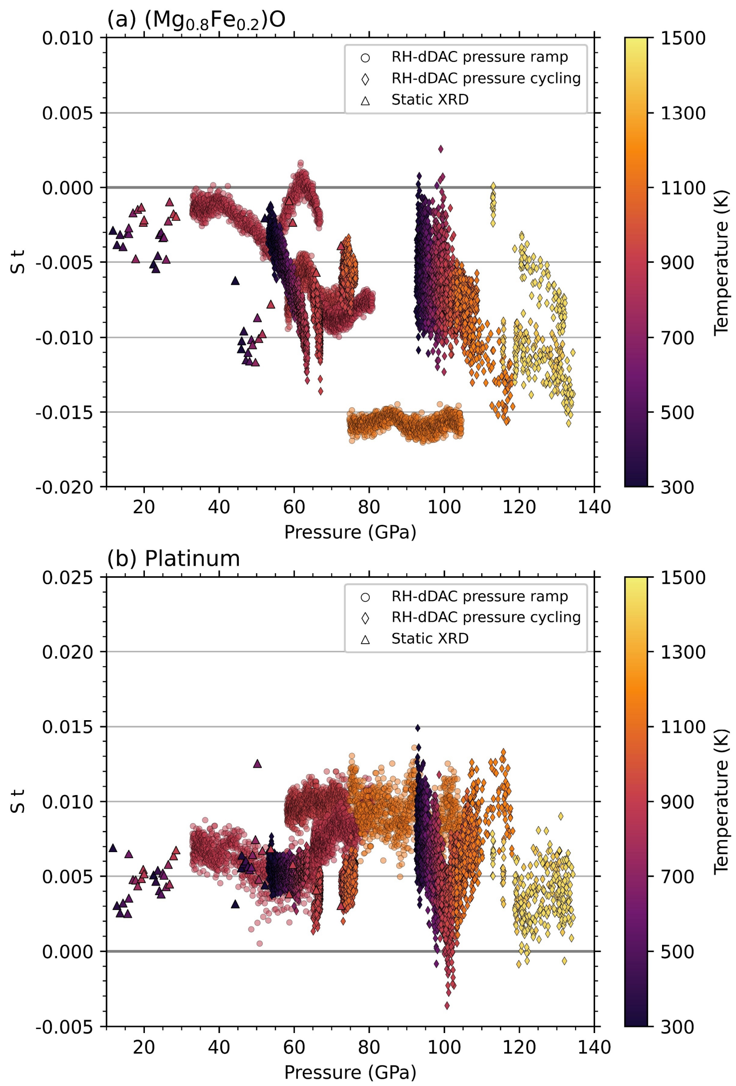

Figure S2. Product of elastic compliance S and uniaxial stress component t as a function of pressure for a) ferropericlase, and b) platinum, obtained from a line-shift analysis of the all data collected in the RH-dDAC. St values can be used as an indicator of the magnitude of deviatoric stress.

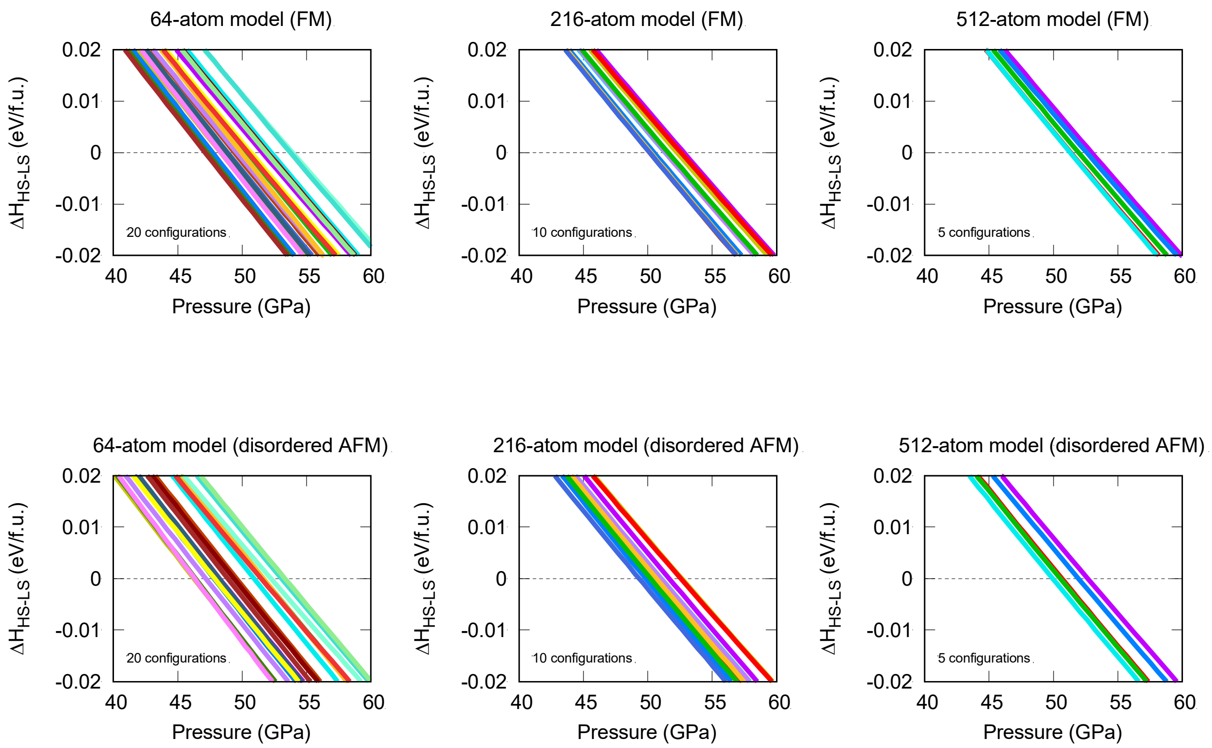

Figure S3. Calculated enthalpy difference between high- and low-spin state for ferropericlase models of different size (from left to right: 64-atoms, 216-atoms and 512-atoms), with different iron arrangements (indicated by different colours). The spin transition occurs at $\Delta \boldsymbol{H_{HS-LS}} = \mathbf{0}$. For the 216-atom models the red line denotes Configuration 1, the green line denotes Configuration 4 and the dark blue line denotes Configuration 10.

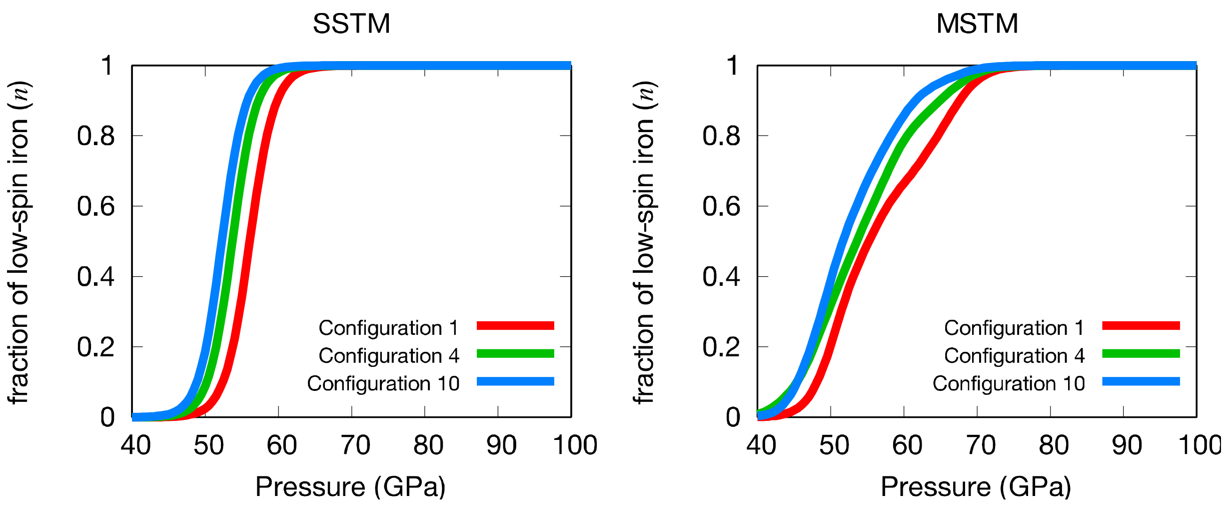

Figure S4. Calculated low-spin fraction at 300K, for models with different iron configurations, using the single spin transition method (SSTM) and multiple spin transition method (MSTM). Even when using a 216-atom model, the arrangement of iron atoms makes a difference to the spin crossover, causing variations in the onset pressure. The MSTM produces a broader spin crossover than the SSTM.

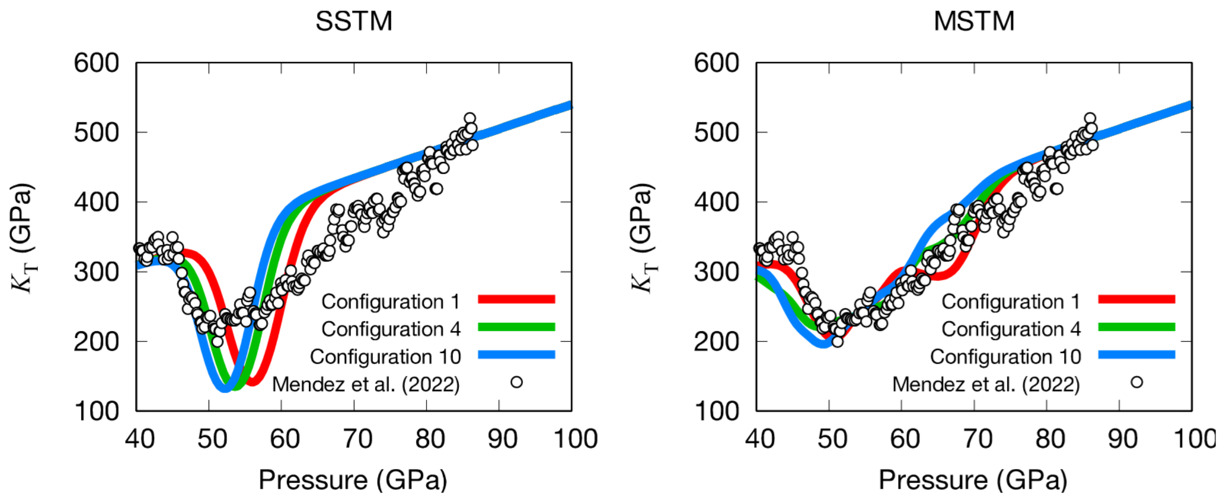

Figure S5. Calculated bulk modulus at 300K, for models with different iron configurations, using the single spin transition method (SSTM) and multiple spin transition method (MSTM). Even when using a 216-atom model, the arrangement of iron atoms makes a difference to the bulk modulus, causing variations in the onset pressure. The MSTM produces a broader spin crossover than the SSTM.

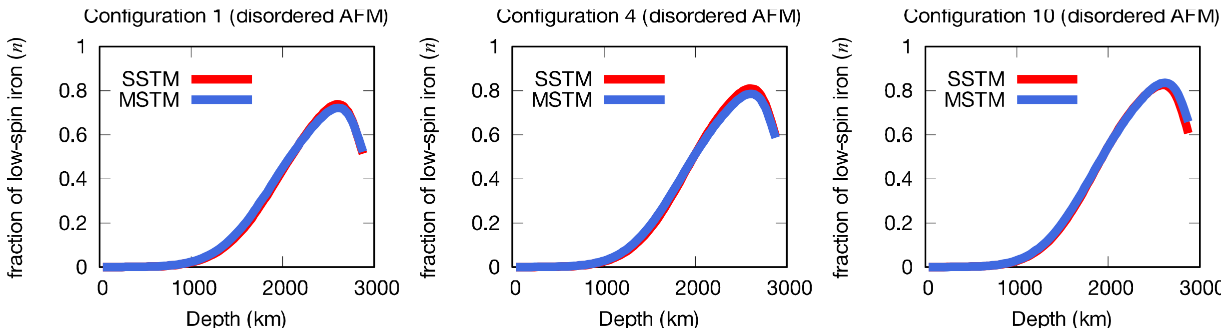

Figure S6. Calculated low-spin fraction along a typical mantle geotherm (Stixrude and Lithgow-Bertelloni, 2011), for models with different iron configurations, using the single spin transition method (SSTM) and multiple spin transition method (MSTM). The arrangement of iron atoms makes a small difference to the spin crossover, causing variations in the onset pressure. In contrast to what is observed at 300K, at lower mantle temperatures, the MSTM and SSTM give very similar results.

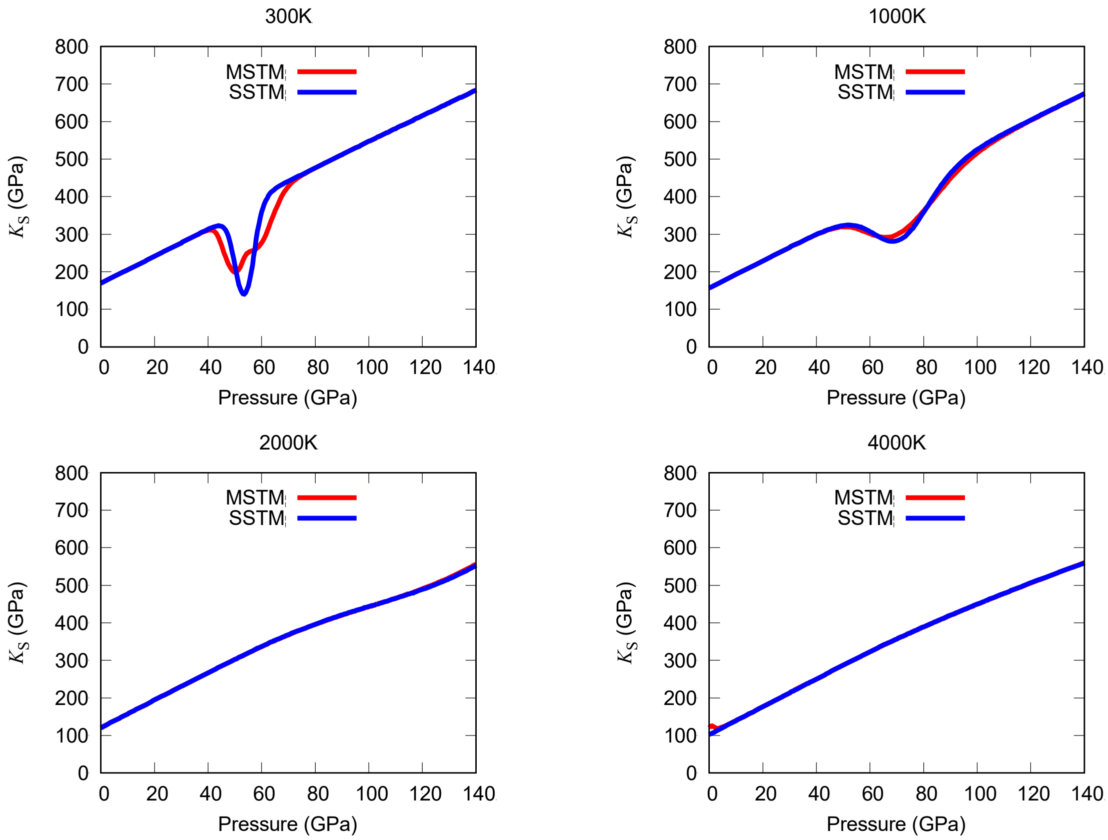

Figure S7. Comparison of estimated values of adiabatic bulk moduli (red lines) calculated using the MSTM and SSTM. Differences are observed at ambient temperature, but almost identical results are obtained above 1000K.

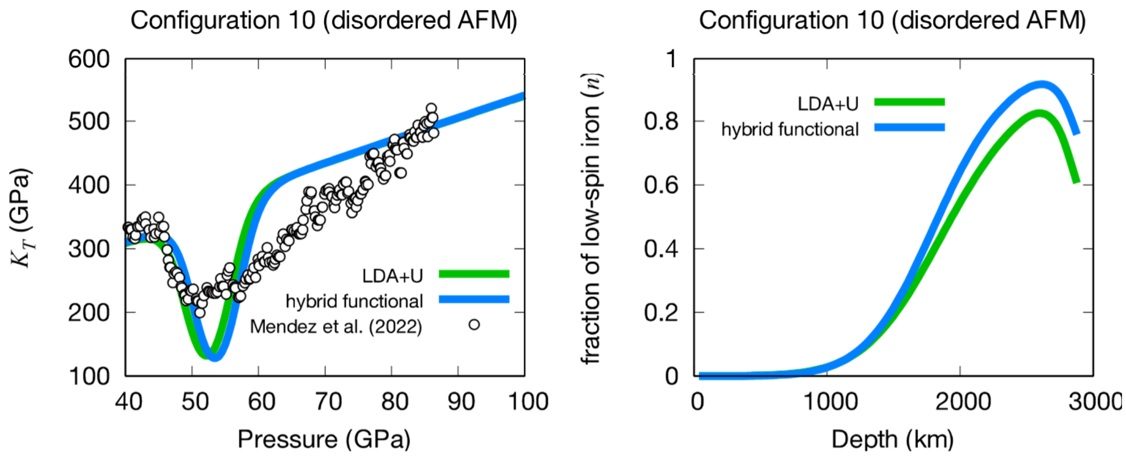

Figure S8. Comparison of results obtained for Configuration 10 using the LDA+U method and hybrid functional comprising LDA with a 0.25 fraction of exact exchange. In both figures the single spin transition method (SSTM) is used and vibrational free energy is neglected. (left) Calculated bulk modulus at 300K. (right) Calculated low-spin fraction along a typical mantle geotherm (Stixrude and Lithgow-Bertelloni, 2011). There is general agreement between the results of both methods, with some small differences at the greatest depths along a mantle geotherm.

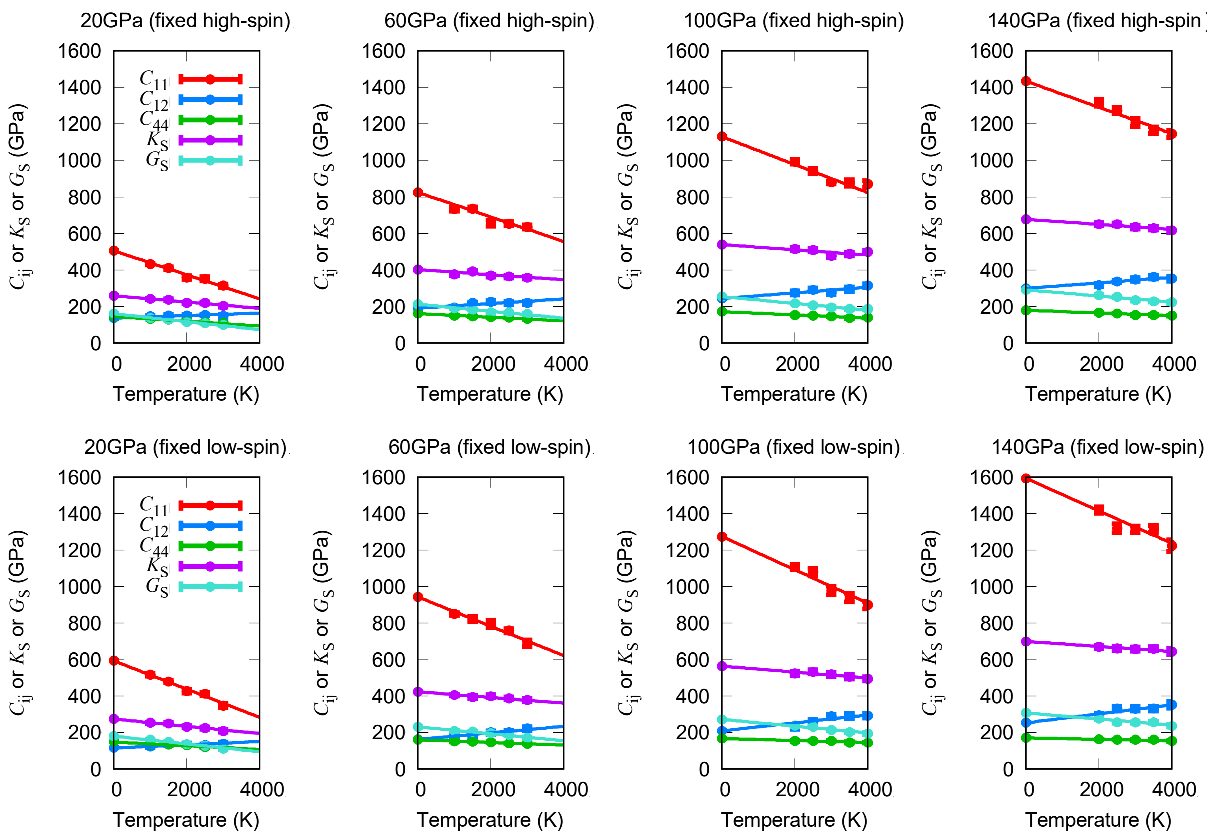

Figure S9. Calculated values of adiabatic elastic constants, bulk and shear moduli (filled circles), from molecular dynamics simulations and corresponding linear fit (solid lines). Note that, pressures exclude the +3.5GPa pressure correction.

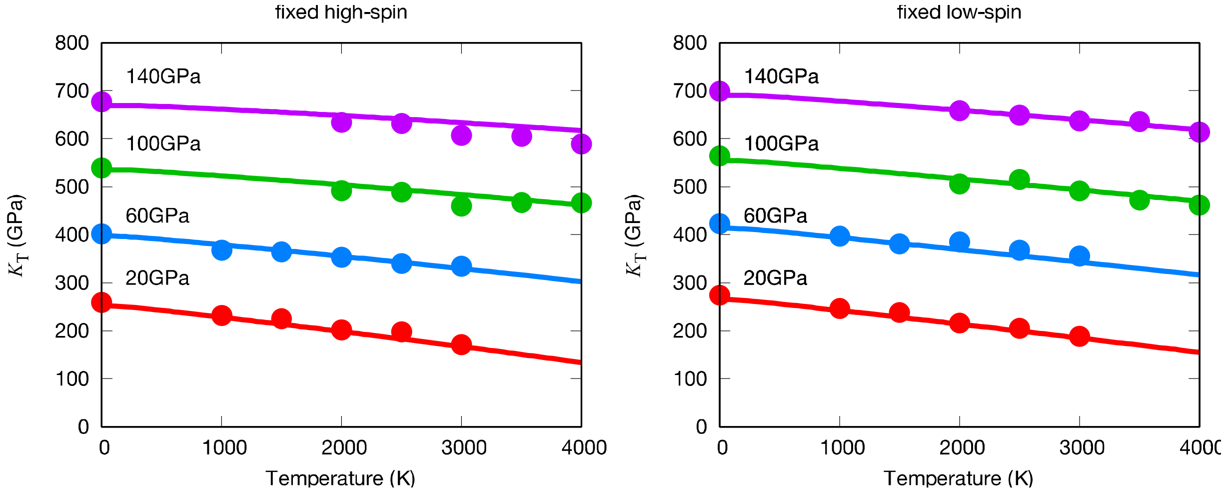

Figure S10. Comparison of isothermal bulk moduli calculated from lattice dynamics calculations (solid lines) and molecular dynamics simulations (filled circles). Error bars are smaller than the symbol size. There is excellent agreement between the two sets of values. Note that, pressures exclude the +3.5GPa pressure correction.

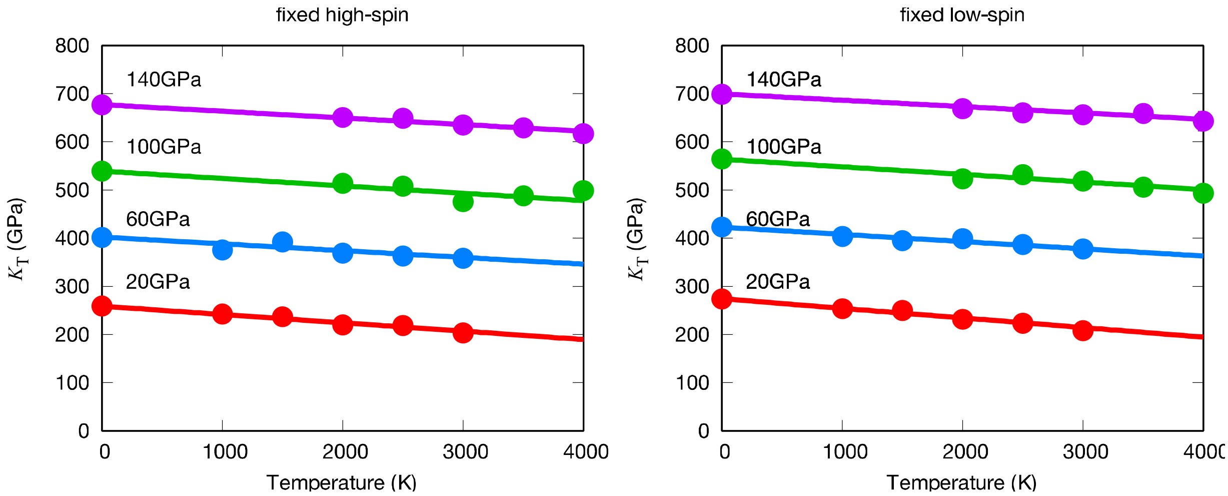

Figure S11. Interpolated values of adiabatic bulk moduli (solid lines), based on those calculated from molecular dynamics simulations (filled circles). Note that, pressures exclude the +3.5GPa pressure correction.

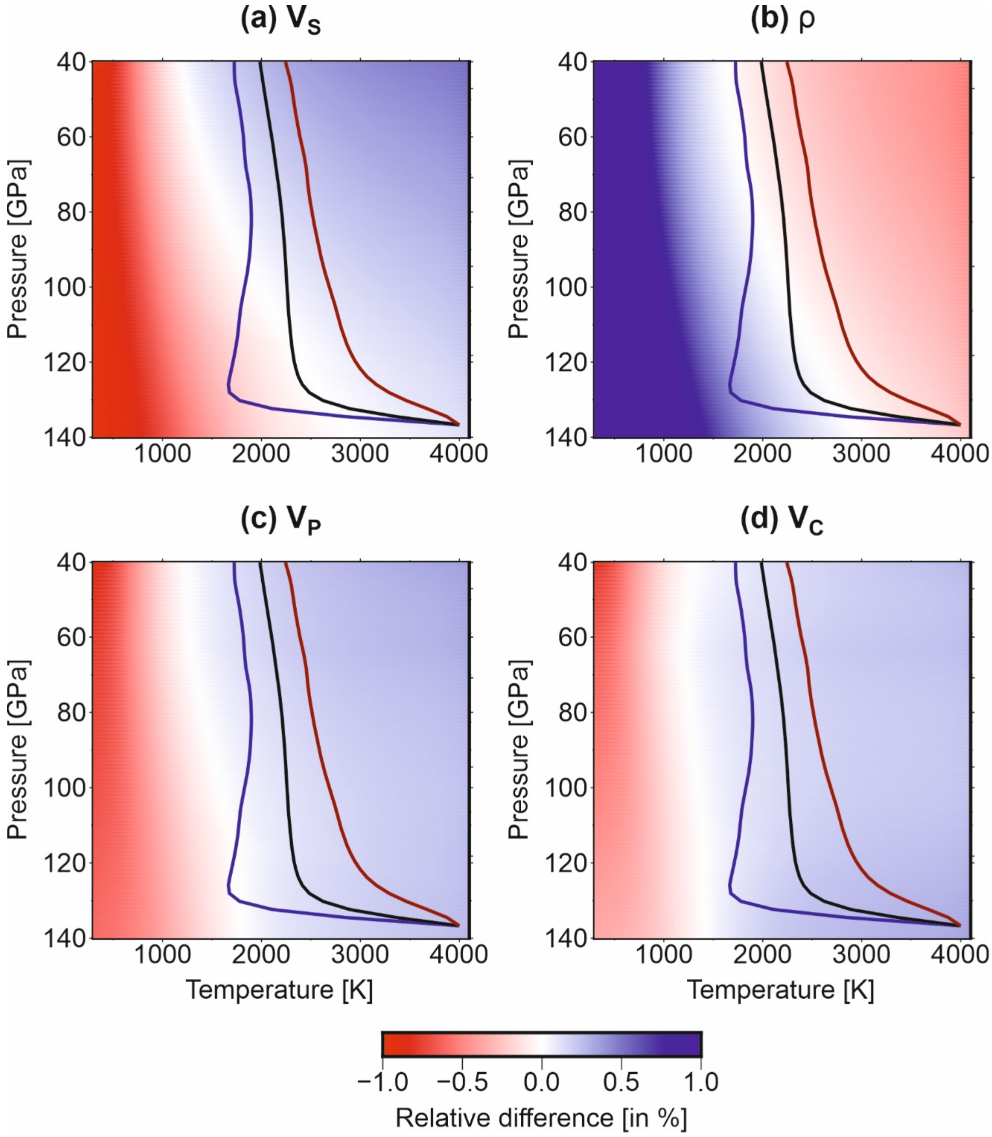

Figure S12. Relative differences in (a) S-wave velocity V_S, (b) density, (c) P-wave velocity V_P, and (d) bulk sound velocity V_C as a function of pressure and temperature, between the pyrolite thermodynamic database from Stixrude and Lithgow-Bertelloni (2011), versus the adapted database obtained by replacing the phase properties of high-spin ferropericlase with the computational results from this study and recalculating the Voigt-Reuss-Hill average. Also shown are a radially averaged geotherm (black) and the range of temperature variations in hot (red) and cold (blue) regions of the mantle (Davies et al., 2012). Along a typical geotherm differences between the databases are less than 0.5 %.

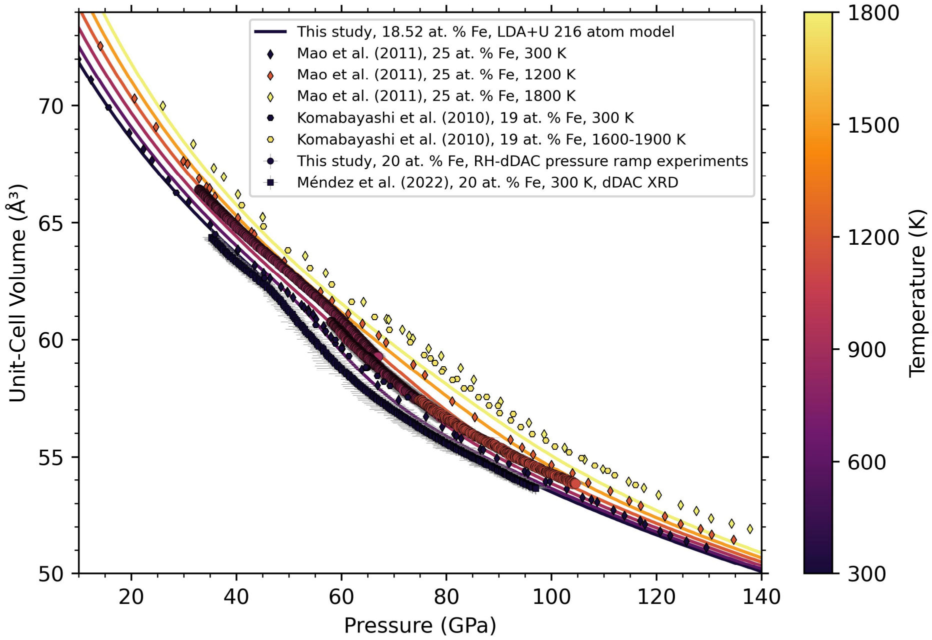

Figure S13. Volume-pressure data collected in the RH-dDAC at high temperature in this study (filled circles), in the dDAC at 300 K (squares, Méndez et al., 2022) and in the laser-heated DAC at high temperature (Mao et al., 2011; Komabayashi et al., 2010, diamonds and hexagons, respectively), together with isotherms predicted from ab-initio calculations (solid lines).

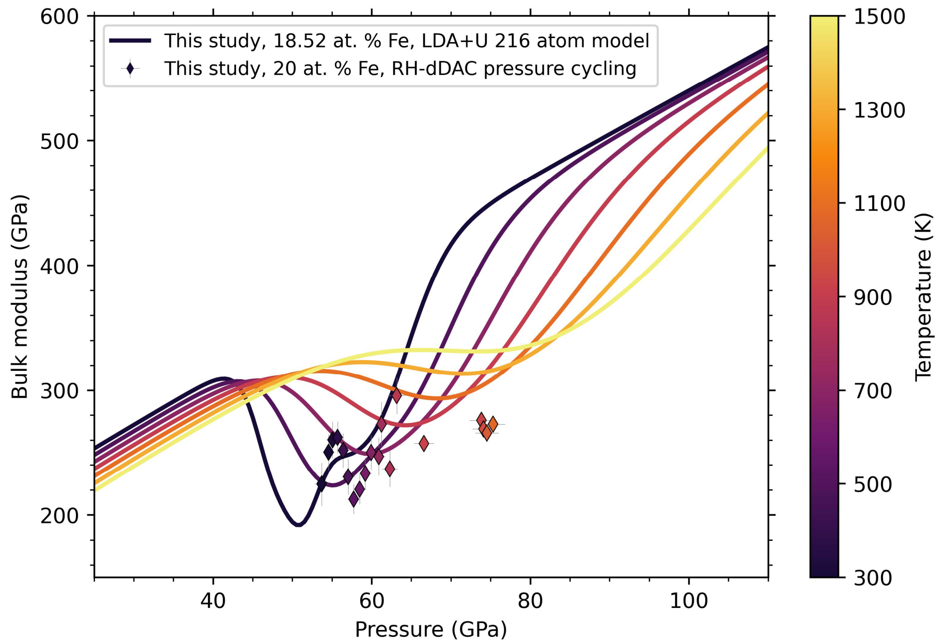

Figure S14. Bulk moduli derived from pressure cycling experiments at selected pressure-temperature conditions, together with isotherms from the lattice dynamics calculations.

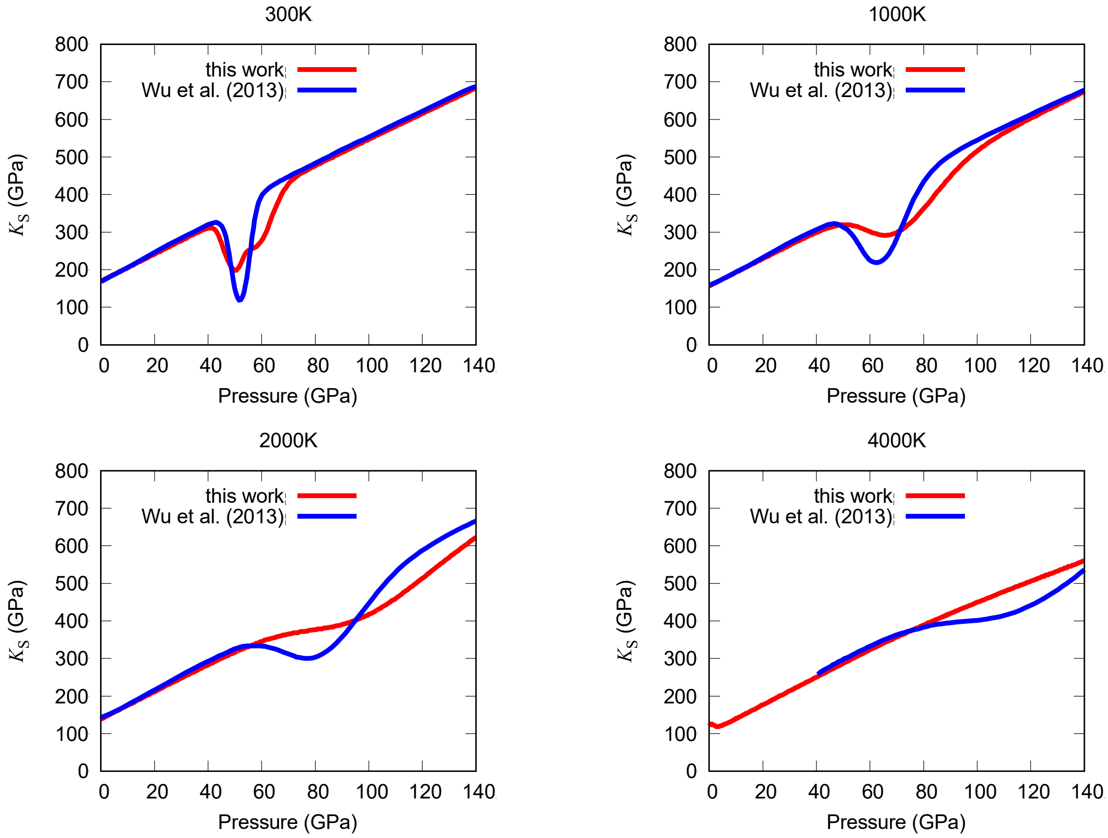

Figure S15. Estimated values of adiabatic bulk moduli (red lines) compared to those reported by Wu et al. (2013) (blue lines). There is excellent agreement at pressures where ferropericlase is in a fully high-spin or low-spin state, but disagreement in regions where a mixed-spin state is stable, indicating that differences are related to the calculation of the fraction of low-spin iron

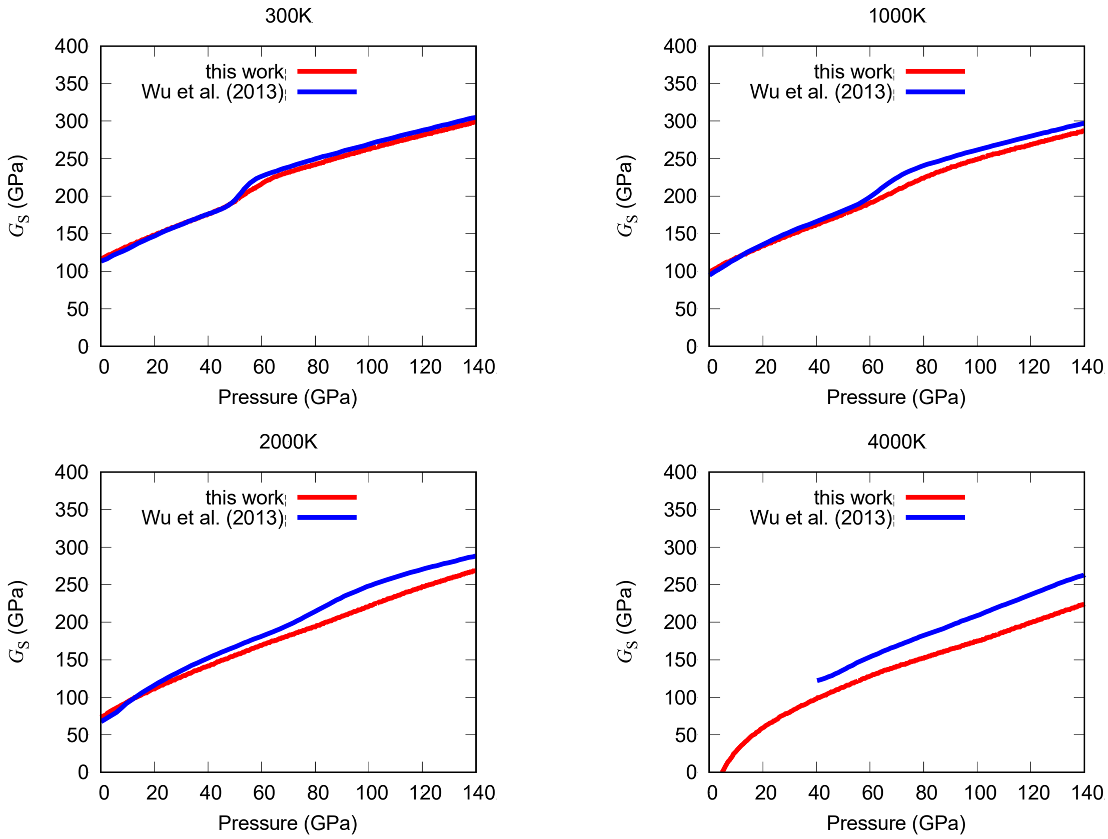

Figure S16. Estimated values of adiabatic shear moduli (red lines) compared to those reported by Wu et al. (2013) (blue lines). There is overall agreement, with moderate differences at the highest temperatures.

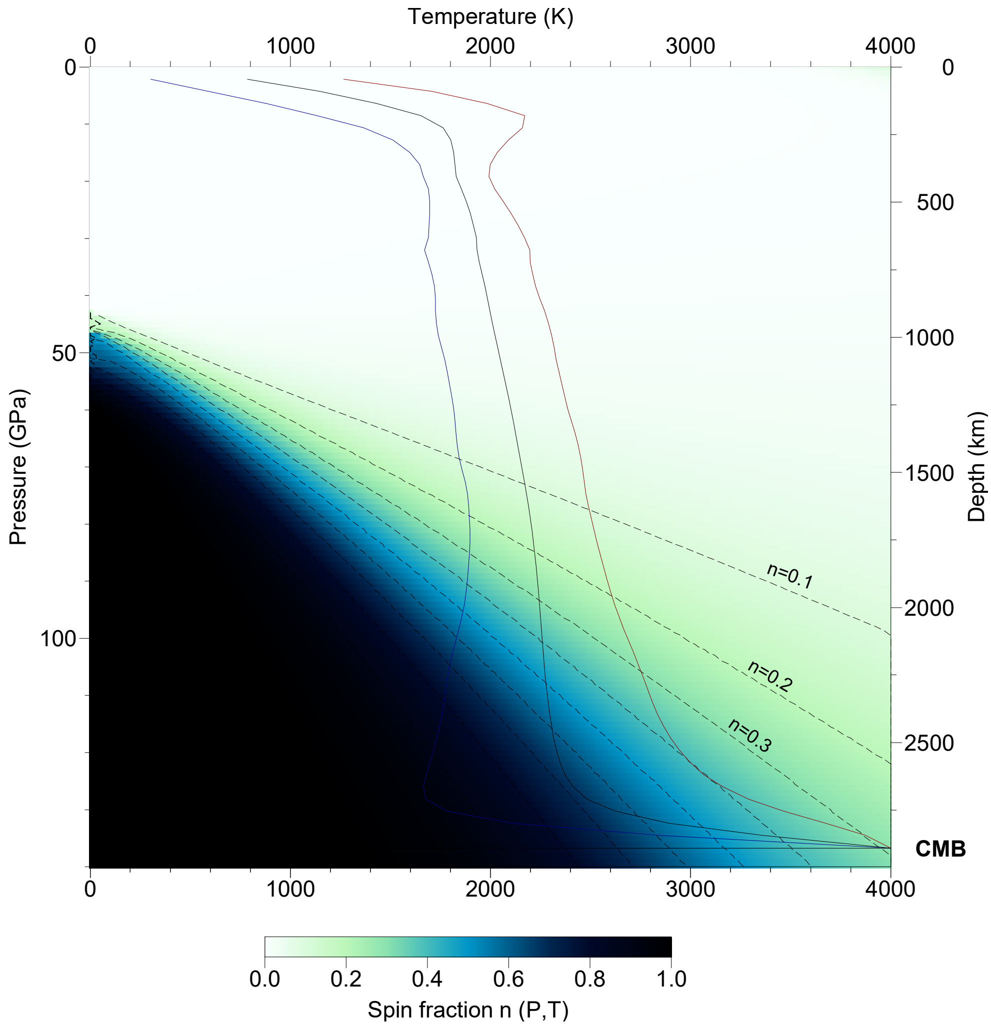

Figure S17. Low-spin fraction n as a function of pressure P and temperature T predicted by our theoretical calculations, indicated by colour and contours. A radially averaged geotherm (black) and the range of temperature variations in hot (red) and cold (blue) regions of the mantle (Davies et al., 2012) are also shown, indicating that full low-spin state is not reached in the lower mantle along a typical geotherm.

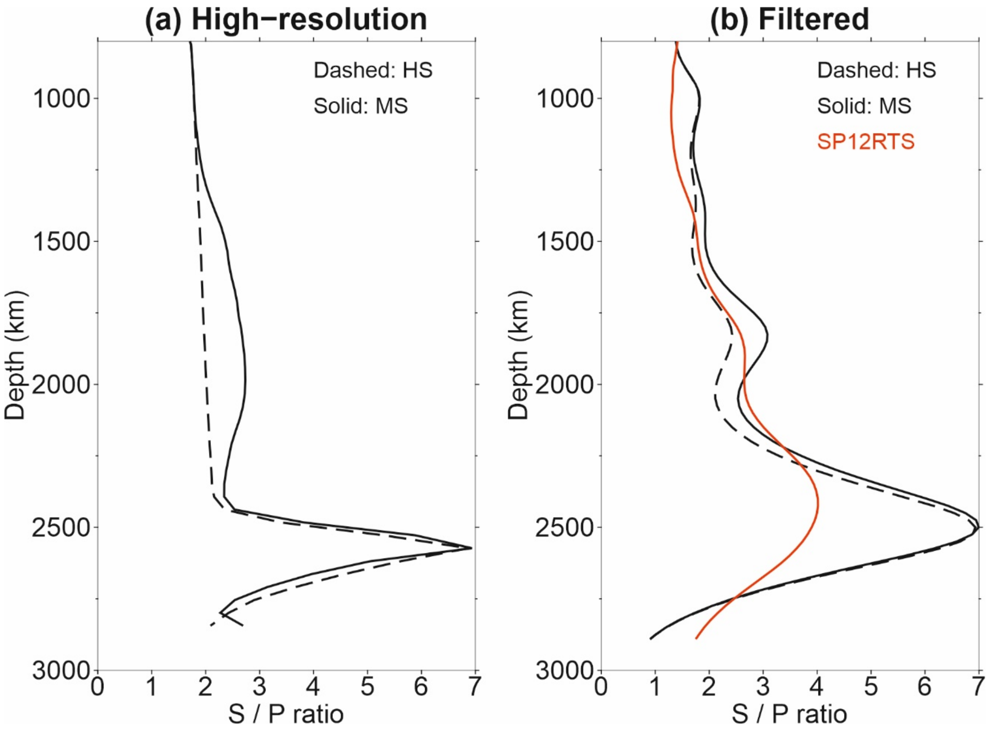

Figure S18. Prediction of radially averaged ratio between variations in V_S and V_P (S / P ratio) along depth profiles in the synthetic tomography models with high-spin HS and mixed-spin MS ferropericlase (dashed and solid lines, respectively). (a) Results without the application of a tomographic filter, showing a moderate positive anomaly in the mid lower mantle produced by the spin crossover. (b) Results of the synthetic models with tomography filtering compared to seismic tomography model SP12RTS (red) (Koelemeijer et al., 2016). The differences between the models are small after filtering and the MS model does not significantly improve the fit with SP12RTS.

Table S1. Summary of experimental runs

Experiment	DAC	T (K)	u (T)	Nr of patterns	Starting P (GPa)	P range (GPa)	Max. compression rate (GPa/s)
Ramp 1	RH 1	895	13.0	1050	32.9	34.2	0.3
Ramp 2	RH 1	927	6.4	1050	58	16.5	0.17
Ramp 3	RH 1	894	3.8	1050	64.9	16	0.18
Ramp 4	RH 2	1131	35.5	1050	74.7	29.9	0.22
Osc 1	RH 1	300	-	100	52.9	1.2	0.46
Osc 2	RH 1	300	-	100	54.0	1.0	0.41
Osc 3	RH 1	325	1.7	100	54.6	0.9	0.36
Osc 4	RH 1	378	1.8	100	55.2	1.0	0.38
Osc 5	RH 1	433	3.8	100	55.9	1.0	0.38
Osc 6	RH 1	479	4.8	100	56.5	1.0	0.40
Osc 7	RH 1	530	6.0	100	57.2	0.9	0.36
Osc 8	RH 1	581	6.5	100	57.9	1.0	0.40
Osc 9	RH 1	624	6.3	100	58.5	1.2	0.48
Osc 10	RH 1	671	6.0	100	59.3	1.1	0.44
Osc 11	RH 1	734	5.3	100	60.2	1.2	0.47
Osc 12	RH 1	777	6.0	100	60.5	1.2	0.47
Osc 13	RH 1	819	6.5	100	61.6	1.1	0.44
Osc 14	RH 1	867	7.8	100	62.3	1.4	0.54
Osc 15	RH 1	927	6.4	100	65.0	2.2	0.88
Osc 16	RH 1	937	6.5	100	72.4	2.9	1.15
Osc 17	RH 1	971	6.5	100	72.7	2.8	1.11
Osc 18	RH 1	1021	7.5	100	72.9	2.9	1.16
Osc 19	RH 1	1070	13.8	100	73.8	2.7	1.10
Osc 20	RH 2	300	-	100	92.4	1.1	0.43
Osc 21	RH 2	327	6.8	100	92.6	1.0	0.40
Osc 22	RH 2	388	7.3	100	93.1	1.9	0.75
Osc 23	RH 2	392	7.0	100	93.2	2.6	1.02
Osc 24	RH 2	443	8.0	100	93.5	2.8	1.12
Osc 25	RH 2	502	10.3	100	94.1	2.6	1.05
Osc 26	RH 2	566	10.8	100	94.7	3.4	1.36
Osc 27	RH 2	592	11.3	100	94.9	3.3	1.33
Osc 28	RH 2	672	14.3	100	95.7	3.1	1.25
Osc 29	RH 2	727	15.3	100	96.7	3.1	1.22
Osc 30	RH 2	759	15.5	100	96.9	3.1	1.26
Osc 31	RH 2	811	17.5	100	97.7	3.1	1.24
Osc 32	RH 2	859	18.3	100	98.4	2.9	1.17
Osc 33	RH 2	910	17.8	100	99.2	3.4	1.36
Osc 34	RH 2	952	13.5	100	100.6	3.2	1.30
Osc 35	RH 2	1000	8.8	100	101.6	3.5	1.40
Osc 36	RH 2	1044	2.0	100	102.3	4.1	1.63
Osc 37	RH 2	1070	4.5	100	103.2	4.3	1.73
Osc 38	RH 2	1133	11.0	100	104.1	4.8	1.90
Osc 39	RH 2	1128	14.3	100	103.2	4.9	1.97
Osc 40	RH 2	1180	17.8	100	106.9	11.4	4.54
Osc 41	RH 2	1392	24.3	100	115.5	16.0	6.40
Osc 42	RH 2	1430	19.3	100	118.7	15.6	6.25
Osc 43	RH 2	1436	6.5	100	112.8	19.3	7.74

Table S2. Initial atomic coordinates of iron atoms in the 216-atom models

	x	*y*	*z*		*x*	*y*	*z*		*x*	*y*	*z*		*x*	*y*	*z*
Configuration 1								*Configuration 2*							
Fe1	1/2	1/3	1/6	**Fe11**	0	2/3	2/3	**Fe1**	1/3	0	2/3	**Fe11**	5/6	0	1/2
Fe2	1/6	1/2	2/3	**Fe12**	5/6	0	1/2	**Fe2**	0	5/6	1/6	**Fe12**	5/6	1/2	1/3
Fe3	1/2	5/6	0	**Fe13**	5/6	1/2	2/3	**Fe3**	2/3	1/2	5/6	**Fe13**	1/2	5/6	0
Fe4	1/6	0	5/6	**Fe14**	1/6	1/2	1/3	**Fe4**	1/6	5/6	0	**Fe14**	2/3	5/6	5/6
Fe5	1/3	1/6	1/6	**Fe15**	0	1/6	1/6	**Fe5**	5/6	5/6	1/3	**Fe15**	2/3	2/3	0
Fe6	1/2	1/6	1/3	**Fe16**	2/3	1/3	2/3	**Fe6**	2/3	1/6	5/6	**Fe16**	5/6	0	5/6
Fe7	2/3	1/6	5/6	**Fe17**	1/2	2/3	1/6	**Fe7**	1/3	2/3	2/3	**Fe17**	1/6	0	1/2
Fe8	5/6	1/6	2/3	**Fe18**	1/2	5/6	2/3	**Fe8**	1/3	1/2	1/6	**Fe18**	1/6	1/2	0
Fe9	1/3	1/3	1/3	**Fe19**	5/6	1/6	1/3	**Fe9**	0	1/6	1/2	**Fe19**	1/6	1/6	1/3
Fe10	1/2	2/3	1/2	**Fe20**	5/6	1/3	1/6	**Fe10**	2/3	5/6	1/6	**Fe20**	0	2/3	0
Configuration 3								*Configuration 4*							
Fe1	2/3	1/6	1/6	**Fe11**	0	2/3	1/3	**Fe1**	1/6	0	1/2	**Fe11**	1/2	0	1/6
Fe2	1/3	0	2/3	**Fe12**	2/3	2/3	1/3	**Fe2**	5/6	1/3	1/6	**Fe12**	1/2	2/3	5/6
Fe3	2/3	1/3	1/3	**Fe13**	2/3	1/6	1/2	**Fe3**	1/2	5/6	0	**Fe13**	1/6	5/6	1/3
Fe4	1/6	0	1/6	**Fe14**	1/2	1/6	2/3	**Fe4**	5/6	0	1/6	**Fe14**	0	5/6	1/6
Fe5	1/2	1/3	1/2	**Fe15**	5/6	1/6	2/3	**Fe5**	1/6	1/3	1/2	**Fe15**	1/2	1/6	1/3
Fe6	1/6	1/2	2/3	**Fe16**	1/3	2/3	0	**Fe6**	5/6	1/6	0	**Fe16**	2/3	1/3	0
Fe7	5/6	1/2	2/3	**Fe17**	0	1/6	5/6	**Fe7**	0	5/6	5/6	**Fe17**	1/2	0	1/2
Fe8	1/6	1/2	0	**Fe18**	1/2	1/6	0	**Fe8**	1/6	1/3	5/6	**Fe18**	1/3	1/2	5/6
Fe9	0	1/3	1/3	**Fe19**	5/6	2/3	1/6	**Fe9**	1/3	1/2	1/2	**Fe19**	1/3	5/6	5/6
Fe10	1/2	5/6	2/3	**Fe20**	1/6	2/3	2/3	**Fe10**	2/3	2/3	1/2	**Fe20**	1/6	1/2	1/3
Configuration 5								*Configuration 6*							
Fe1	0	1/2	1/2	**Fe11**	2/3	0	1/3	**Fe1**	2/3	5/6	1/2	**Fe11**	1/2	1/6	1/3
Fe2	0	2/3	0	**Fe12**	2/3	1/2	1/6	**Fe2**	2/3	1/3	0	**Fe12**	0	1/6	1/6
Fe3	1/2	1/6	2/3	**Fe13**	0	5/6	1/2	**Fe3**	1/3	0	2/3	**Fe13**	1/6	1/6	2/3
Fe4	1/6	0	1/6	**Fe14**	2/3	1/6	1/2	**Fe4**	5/6	2/3	5/6	**Fe14**	5/6	1/6	1/3
Fe5	0	2/3	2/3	**Fe15**	1/2	2/3	1/6	**Fe5**	1/3	1/3	2/3	**Fe15**	1/2	1/2	2/3
Fe6	1/3	1/3	2/3	**Fe16**	5/6	1/6	0	**Fe6**	1/2	2/3	5/6	**Fe16**	1/3	1/3	0
Fe7	1/3	1/6	1/6	**Fe17**	1/3	1/2	5/6	**Fe7**	0	1/6	5/6	**Fe17**	1/6	1/2	2/3
Fe8	1/3	1/3	1/3	**Fe18**	5/6	0	5/6	**Fe8**	1/6	1/6	1/3	**Fe18**	5/6	1/3	1/2
Fe9	1/6	1/2	2/3	**Fe19**	1/2	0	1/6	**Fe9**	5/6	0	1/2	**Fe19**	2/3	1/2	1/2
Fe10	1/6	1/6	1/3	**Fe20**	1/6	5/6	2/3	**Fe10**	0	5/6	1/2	**Fe20**	1/2	0	5/6
Configuration 7								*Configuration 8*							
Fe1	5/6	5/6	0	**Fe11**	0	1/3	0	**Fe1**	5/6	2/3	5/6	**Fe11**	1/6	1/3	5/6
Fe2	1/3	2/3	2/3	**Fe12**	1/6	1/6	2/3	**Fe2**	0	1/3	2/3	**Fe12**	0	2/3	2/3
Fe3	2/3	2/3	0	**Fe13**	1/3	1/6	1/2	**Fe3**	1/3	1/6	1/2	**Fe13**	5/6	1/6	0
Fe4	5/6	2/3	1/6	**Fe14**	0	1/2	5/6	**Fe4**	1/6	1/2	1/3	**Fe14**	0	2/3	0
Fe5	1/6	1/6	0	**Fe15**	1/2	2/3	5/6	**Fe5**	5/6	0	1/6	**Fe15**	0	5/6	1/2
Fe6	2/3	5/6	1/2	**Fe16**	1/6	5/6	0	**Fe6**	0	5/6	5/6	**Fe16**	5/6	2/3	1/2
Fe7	1/2	2/3	1/2	**Fe17**	1/6	2/3	5/6	**Fe7**	1/6	5/6	1/3	**Fe17**	1/6	1/6	0
Fe8	1/2	5/6	1/3	**Fe18**	1/2	0	1/2	**Fe8**	1/2	1/3	5/6	**Fe18**	2/3	0	1/3
Fe9	1/2	1/2	1/3	**Fe19**	1/3	1/3	1/3	**Fe9**	5/6	0	5/6	**Fe19**	5/6	1/2	1/3
Fe10	5/6	1/6	2/3	**Fe20**	5/6	2/3	1/2	**Fe10**	1/3	0	2/3	**Fe20**	1/6	0	5/6
Configuration 9								*Configuration 10*							
Fe1	5/6	1/3	5/6	**Fe11**	1/3	0	0	**Fe1**	1/3	0	2/3	**Fe11**	1/6	1/6	2/3
Fe2	5/6	1/3	1/6	**Fe12**	1/2	1/3	1/6	**Fe2**	0	5/6	1/2	**Fe12**	1/2	0	1/6
Fe3	0	1/2	1/6	**Fe13**	1/2	5/6	0	**Fe3**	2/3	5/6	1/2	**Fe13**	0	1/2	5/6
Fe4	1/2	1/3	1/2	**Fe14**	2/3	1/3	2/3	**Fe4**	5/6	1/3	5/6	**Fe14**	1/2	1/6	0
Fe5	1/3	1/6	5/6	**Fe15**	1/6	0	1/6	**Fe5**	5/6	0	5/6	**Fe15**	5/6	1/6	1/3
Fe6	1/3	1/2	1/6	**Fe16**	5/6	5/6	2/3	**Fe6**	2/3	1/3	0	**Fe16**	1/6	1/2	2/3
Fe7	1/2	5/6	2/3	**Fe17**	1/6	2/3	5/6	**Fe7**	0	2/3	1/3	**Fe17**	5/6	1/2	2/3
Fe8	5/6	1/2	1/3	**Fe18**	2/3	1/3	0	**Fe8**	0	1/6	1/6	**Fe18**	1/2	0	1/2
Fe9	1/6	1/6	1/3	**Fe19**	5/6	1/6	2/3	**Fe9**	1/2	1/2	1/3	**Fe19**	1/3	0	1/3
Fe10	5/6	5/6	1/3	**Fe20**	5/6	0	5/6	**Fe10**	1/2	1/6	2/3	**Fe20**	5/6	5/6	0

Table S3. Initial atomic coordinates of iron atoms in the 512-atom models

		x	*y*	*z*		*x*	*y*	*z*		*x*	*y*	*z*		*x*	*y*	*z*
Conf. 1	**Fe1**	0.375	0.375	0.000	**Fe13**	0.500	0.375	0.625	**Fe25**	0.625	0.250	0.125	**Fe37**	0.375	0.250	0.875
	Fe2	0500	0.750	0.250	**Fe14**	0.125	0.375	0.250	**Fe26**	0.250	0.125	0.625	**Fe38**	0.375	0.750	0.625
	Fe3	0.750	0.000	0.250	**Fe15**	0.750	0.500	0.000	**Fe27**	0.500	0.125	0.375	**Fe39**	0.250	0.625	0.125
	Fe4	0.500	0.750	0.500	**Fe16**	0.750	0.250	0.250	**Fe28**	0.875	0.750	0.125	**Fe40**	0.250	0.500	0.250
	Fe5	0.625	0.000	0.125	**Fe17**	0.000	0.500	0.500	**Fe29**	0.625	0.875	0.750	**Fe41**	0.125	0.500	0.875
	Fe6	0.875	0.250	0.875	**Fe18**	0.375	0.500	0.875	**Fe30**	0.625	0.375	0.250	**Fe42**	0.875	0.625	0.000
	Fe7	0.000	0.500	0.000	**Fe19**	0.625	0.250	0.375	**Fe31**	0.375	0.500	0.625	**Fe43**	0.750	0.250	0.500
	Fe8	0.500	0.875	0.875	**Fe20**	0.750	0.750	0.500	**Fe32**	0.000	0.250	0.000	**Fe44**	0.500	0.875	0.625
	Fe9	0.750	0.375	0.625	**Fe21**	0.375	0.000	0.875	**Fe33**	0.125	0.000	0.375	**Fe45**	0.000	0.250	0.500
	Fe10	0.750	0.625	0.375	**Fe22**	0.000	0.875	0.875	**Fe34**	0.000	0.125	0.875	**Fe46**	0.000	0.750	0.500
	Fe11	0.000	0.250	0.250	**Fe23**	0.500	0.750	0.750	**Fe35**	0.125	0.875	0.750	**Fe47**	0.125	0.750	0.125
	Fe12	0.625	0.625	0.250	**Fe24**	0.375	0.750	0.125	**Fe36**	0.625	0.875	0.250	**Fe48**	0.500	0.250	0.000
Conf. 2	**Fe1**	0.625	0.875	0.250	**Fe13**	0.625	0.125	0.250	**Fe25**	0.625	0.250	0.375	**Fe37**	0.500	0.375	0.125
	Fe2	0.250	0.500	0.750	**Fe14**	0.125	0.250	0.625	**Fe26**	0.875	0.250	0.375	**Fe38**	0.125	0.000	0.375
	Fe3	0.000	0.750	0.750	**Fe15**	0.875	0.500	0.375	**Fe27**	0.250	0.625	0.625	**Fe39**	0.375	0.500	0.625
	Fe4	0.500	0.125	0.625	**Fe16**	0.500	0.875	0.375	**Fe28**	0.875	0.375	0.000	**Fe40**	0.750	0.250	0.500
	Fe5	0.500	0.000	0.500	**Fe17**	0.625	0.375	0.750	**Fe29**	0.250	0.875	0.375	**Fe41**	0.875	0.625	0.000
	Fe6	0.000	0.875	0.375	**Fe18**	0.500	0.500	0.500	**Fe30**	0.500	0.750	0.250	**Fe42**	0.375	0.375	0.250
	Fe7	0.125	0.250	0.125	**Fe19**	0.250	0.250	0.750	**Fe31**	0.500	0.125	0.125	**Fe43**	0.875	0.875	0.000
	Fe8	0.125	0.750	0.375	**Fe20**	0.750	0.000	0.250	**Fe32**	0.000	0.625	0.375	**Fe44**	0.000	0.125	0.125
	Fe9	0.750	0.625	0.375	**Fe21**	0.250	0.250	0.500	**Fe33**	0.250	0.625	0.875	**Fe45**	0.875	0.375	0.500
	Fe10	0.125	0.375	0.000	**Fe22**	0.125	0.250	0.375	**Fe34**	0.375	0.250	0.625	**Fe46**	0.500	0.000	0.250
	Fe11	0.250	0.125	0.125	**Fe23**	0.500	0.500	0.750	**Fe35**	0.750	0.000	0.000	**Fe47**	0.500	0.375	0.625
	Fe12	0.125	0.125	0.500	**Fe24**	0.875	0.000	0.625	**Fe36**	0.875	0.750	0.625	**Fe48**	0.875	0.000	0.125
Conf. 3	**Fe1**	0.375	0.875	0.750	**Fe13**	0.500	0.875	0.375	**Fe25**	0.875	0.250	0.875	**Fe37**	0.375	0.500	0.625
	Fe2	0.125	0.625	0.250	**Fe14**	0.625	0.875	0.250	**Fe26**	0.625	0.500	0.875	**Fe38**	0.875	0.250	0.625
	Fe3	0.250	0.250	0.000	**Fe15**	0.250	0.375	0.625	**Fe27**	0.250	0.000	0.000	**Fe39**	0.125	0.000	0.125
	Fe4	0.125	0.375	0.750	**Fe16**	0.125	0.875	0.000	**Fe28**	0.375	0.875	0.250	**Fe40**	0.125	0.250	0.125
	Fe5	0.000	0.875	0.375	**Fe17**	0.125	0.125	0.500	**Fe29**	0.375	0.000	0.375	**Fe41**	0.375	0.000	0.625
	Fe6	0.500	0.750	0.000	**Fe18**	0.375	0.500	0.875	**Fe30**	0.500	0.500	0.000	**Fe42**	0.125	0.750	0.375
	Fe7	0.250	0.375	0.125	**Fe19**	0.000	0.000	0.250	**Fe31**	0.875	0.125	0.750	**Fe43**	0.125	0.375	0.250
	Fe8	0.750	0.250	0.000	**Fe20**	0.750	0.750	0.000	**Fe32**	0.875	0.750	0.125	**Fe44**	0.125	0.000	0.875
	Fe9	0.000	0.875	0.625	**Fe21**	0.125	0.500	0.625	**Fe33**	0.875	0.000	0.375	**Fe45**	0.625	0.875	0.500
	Fe10	0.625	0.875	0.000	**Fe22**	0.500	0.625	0.375	**Fe34**	0.375	0.125	0.500	**Fe46**	0.375	0.750	0.375
	Fe11	0.750	0.500	0.750	**Fe23**	0.875	0.125	0.000	**Fe35**	0.125	0.500	0.125	**Fe47**	0.000	0.370	0.125
	Fe12	0.250	0.000	0.250	**Fe24**	0.000	0.750	0.500	**Fe36**	0.500	0.375	0.125	**Fe48**	0.000	0.625	0.625
Conf. 4	**Fe1**	0.000	0.750	0.250	**Fe13**	0.875	0.625	0.000	**Fe25**	0.500	0.000	0.000	**Fe37**	0.625	0.375	0.250
	Fe2	0.875	0.125	0.750	**Fe14**	0.375	0.500	0.875	**Fe26**	0.250	0.875	0.125	**Fe38**	0.750	0.500	0.750
	Fe3	0.125	0.250	0.375	**Fe15**	0.875	0.750	0.125	**Fe27**	0.125	0.875	0.250	**Fe39**	0.250	0.250	0.250
	Fe4	0.125	0.000	0.125	**Fe16**	0.875	0.000	0.875	**Fe28**	0.875	0.375	0.00	**Fe40**	0.000	0.875	0.625
	Fe5	0.250	0.125	0.375	**Fe17**	0.375	0.000	0.625	**Fe29**	0.250	0.625	0.625	**Fe41**	0.625	0.875	0.000
	Fe6	0.625	0.750	0.625	**Fe18**	0.125	0.750	0.125	**Fe30**	0.250	0.250	0.000	**Fe42**	0.000	0.250	0.500
	Fe7	0.000	0.375	0.374	**Fe19**	0.875	0.250	0.625	**Fe31**	0.000	0.875	0.125	**Fe43**	0.250	0.625	0.875
	Fe8	0.250	0.875	0.875	**Fe20**	0.125	0.500	0.125	**Fe32**	0.000	0.250	0.250	**Fe44**	0.500	0.750	0.500
	Fe9	0.625	0.500	0.125	**Fe21**	0.125	0.125	0.000	**Fe33**	0.375	0.875	0.750	**Fe45**	0.500	0.000	0.500
	Fe10	0.500	0.375	0.625	**Fe22**	0.625	0.750	0.375	**Fe34**	0.750	0.250	0.500	**Fe46**	0.875	0.875	0.750
	Fe11	0.875	0.750	0.375	**Fe23**	0.625	0.750	0.875	**Fe35**	0.250	0.125	0.125	**Fe47**	0.750	0.750	0.000
	Fe12	0.125	0.625	0.250	**Fe24**	0.625	0.500	0.875	**Fe36**	0.250	0.750	0.500	**Fe48**	0.750	0.750	0.125
Conf. 5	**Fe1**	0.125	0.750	0.375	**Fe13**	0.125	0.375	0.750	**Fe25**	0.125	0.875	0.500	**Fe37**	0.875	0.250	0.375
	Fe2	0.750	0.625	0.625	**Fe14**	0.500	0.500	0.250	**Fe26**	0.000	0.250	0.500	**Fe38**	0.875	0.750	0.125
	Fe3	0.875	0.375	0.250	**Fe15**	0.375	0.625	0.750	**Fe27**	0.500	0.750	0.500	**Fe39**	0.750	0.000	0.000
	Fe4	0.250	0.375	0.125	**Fe16**	0.500	0.000	0.750	**Fe28**	0.250	0.750	0.500	**Fe40**	0.375	0.500	0.125
	Fe5	0.250	0.000	0.750	**Fe17**	0.625	0.875	0.75	**Fe29**	0.000	0.750	0.750	**Fe41**	0.625	0.375	0.500
	Fe6	0.375	0.500	0.625	**Fe18**	0.750	0.875	0.875	**Fe30**	0.375	0.375	0.750	**Fe42**	0.375	0.250	0.875
	Fe7	0.750	0.375	0.875	**Fe19**	0.875	0.875	0.250	**Fe31**	0.250	0.500	0.500	**Fe43**	0.750	0.125	0.625
	Fe8	0.500	0.500	0.00	**Fe20**	0.000	0.750	0.000	**Fe32**	0.000	0.875	0.625	**Fe44**	0.875	0.250	0.125
	Fe9	0.625	0.000	0.125	**Fe21**	0.625	0.500	0.375	**Fe33**	0.500	0.625	0.875	**Fe45**	0.125	0.000	0.375
	Fe10	0.125	0.750	0.125	**Fe22**	0.125	0.125	0.500	**Fe34**	0.375	0.500	0.875	**Fe46**	0.250	0.750	0.00
	Fe11	0.500	0.750	0.000	**Fe23**	0.375	0.750	0.375	**Fe35**	0.750	0.500	0.500	**Fe47**	0.625	0.500	0.875
	Fe12	0.250	0.250	0.750	**Fe24**	0.250	0.875	0.625	**Fe36**	0.875	0.250	0.875	**Fe48**	0.000	0625	0.375

Table S4. Calculated successive stable mixed-spin states for Configurations 1, 4 and 10, when going from high to low-spin, as pressure is increased. Note that, -4 = high spin (spin down magnetic moment), 4 = high spin (spin up magnetic moment), and 0 = low-spin (non-magnetic).

Spin State	Fe																			
	1	**2**	**3**	**4**	**5**	**6**	**7**	**8**	**9**	**10**	**11**	**12**	**13**	**14**	**15**	**16**	**17**	**18**	**19**	**20**
Configuration 1																				
1	-4	-4	-4	-4	-4	-4	-4	-4	-4	-4	4	4	4	4	4	4	4	4	4	4
2	-4	-4	-4	0	-4	-4	-4	-4	-4	-4	4	4	4	4	4	4	4	4	4	4
3	-4	0	-4	0	-4	-4	-4	-4	-4	-4	4	4	4	4	4	4	4	4	4	4
4	-4	0	0	0	-4	-4	-4	-4	-4	-4	4	4	4	4	4	4	4	4	4	4
5	-4	0	0	0	-4	-4	-4	-4	-4	0	4	4	4	4	4	4	4	4	4	4
6	-4	0	0	0	0	-4	-4	-4	-4	0	0	4	4	4	4	0	4	4	4	4
7	-4	0	0	0	0	-4	-4	-4	-4	0	0	0	4	0	4	0	4	4	4	4
8	-4	0	0	0	0	-4	0	0	-4	0	0	0	4	0	4	0	0	0	4	4
9	-4	0	0	0	0	-4	0	0	-4	0	0	0	4	0	4	0	0	0	4	0
10	-4	0	0	0	0	-4	0	0	-4	0	0	0	4	0	0	0	0	0	4	0
11	-4	0	0	0	0	-4	0	0	-4	0	0	0	4	0	0	0	0	0	0	0
12	-4	0	0	0	0	-4	0	0	-4	0	0	0	0	0	0	0	0	0	0	0
13	0	0	0	0	0	0	0	0	0	0	0	0	0	0	0	0	0	0	0	0
Configuration 4																				
1	-4	-4	-4	-4	-4	-4	-4	-4	-4	-4	4	4	4	4	4	4	4	4	4	4
2	-4	-4	-4	-4	-4	-4	-4	0	-4	-4	4	4	4	4	4	4	4	4	4	4
3	-4	-4	-4	-4	-4	-4	-4	0	-4	0	4	4	4	4	4	4	4	4	4	4
4	0	-4	-4	-4	-4	-4	-4	0	-4	0	4	4	4	4	4	4	4	4	4	4
5	0	0	-4	-4	-4	-4	-4	0	-4	0	4	4	4	4	4	4	4	4	4	4
6	0	0	0	-4	-4	-4	-4	0	-4	0	4	4	4	4	4	4	4	4	4	4
7	0	0	0	-4	-4	-4	-4	0	-4	0	4	4	4	4	4	4	4	4	4	0
8	0	0	0	-4	-4	-4	0	0	-4	0	4	4	4	4	4	4	4	4	4	0
9	0	0	0	-4	-4	-4	0	0	-4	0	0	4	4	4	0	0	4	4	4	0
10	0	0	0	-4	-4	-4	0	0	-4	0	0	4	4	4	0	0	4	0	4	0
11	0	0	0	-4	-4	0	0	0	-4	0	0	4	4	4	0	0	4	0	4	0
12	0	0	0	-4	-4	0	0	0	-4	0	0	4	4	0	0	0	4	0	4	0
13	0	0	0	-4	-4	0	0	0	-4	0	0	0	4	0	0	0	4	0	4	0
14	0	0	0	-4	-4	0	0	0	-4	0	0	0	0	0	0	0	4	0	4	0
15	0	0	0	-4	-4	0	0	0	0	0	0	0	0	0	0	0	4	0	4	0
16	0	0	0	-4	-4	0	0	0	0	0	0	0	0	0	0	0	0	0	4	0
17	0	0	0	-4	0	0	0	0	0	0	0	0	0	0	0	0	0	0	4	0
18	0	0	0	-4	0	0	0	0	0	0	0	0	0	0	0	0	0	0	0	0
19	0	0	0	0	0	0	0	0	0	0	0	0	0	0	0	0	0	0	0	0
Configuration 10																				
1	-4	-4	-4	-4	-4	-4	-4	-4	-4	-4	4	4	4	4	4	4	4	4	4	4
2	-4	-4	-4	-4	0	-4	-4	-4	0	-4	0	4	4	4	4	4	4	4	4	4
3	-4	-4	-4	-4	0	-4	-4	0	0	-4	0	4	4	4	4	4	4	4	4	4
4	-4	-4	0	-4	0	-4	0	0	0	-4	0	4	4	4	0	4	0	4	4	0
5	-4	-4	0	-4	0	-4	0	0	0	-4	0	4	4	4	0	4	0	0	4	0
6	-4	-4	0	-4	0	0	0	0	0	-4	0	4	4	4	0	4	0	0	4	0
7	-4	-4	0	-4	0	0	0	0	0	-4	0	4	4	4	0	4	0	0	0	0
8	-4	0	0	-4	0	0	0	0	0	-4	0	4	4	4	0	4	0	0	0	0
9	-4	0	0	-4	0	0	0	0	0	-4	0	4	0	4	0	4	0	0	0	0
10	-4	0	0	-4	0	0	0	0	0	-4	0	4	0	0	0	4	0	0	0	0
11	-4	0	0	0	0	0	0	0	0	-4	0	4	0	0	0	4	0	0	0	0
12	-4	0	0	0	0	0	0	0	0	-4	0	0	0	0	0	4	0	0	0	0
13	-4	0	0	0	0	0	0	0	0	-4	0	0	0	0	0	0	0	0	0	0
14	0	0	0	0	0	0	0	0	0	-4	0	0	0	0	0	0	0	0	0	0
15	0	0	0	0	0	0	0	0	0	0	0	0	0	0	0	0	0	0	0	0

Table S5. Calculated isothermal elastic constants, bulk moduli, shear moduli and density, from molecular dynamics simulations. Note that, pressures exclude the +3.5 GPa pressure correction. Uncertainties are the standard error of the mean.

P (GPa)	*T* (K)	C_{11} (GPa)	C_{12} (GPa)	C_{44} (GPa)	*K* (GPa)	*G* (GPa)	*ρ* (kgm^{-3})
high-spin state							
20	0	505±0	136±0	145±0	259±0	160±0	4600
20	1000	423±5	137±4	132±0	232±3	136±1	4471
20	1500	399±7	138±5	127±1	225±4	128±2	4416
20	2000	340±9	133±4	123±1	202±4	115±2	4350
20	2500	330±10	132±4	113±1	198±5	108±2	4288
20	3000	282±7	115±6	110±2	171±5	99±2	4192
60	0	825±0	191±0	161±0	402±0	212±0	5201
60	1000	726±11	188±5	149±1	368±5	189±2	5116
60	1500	692±9	200±4	146±1	364±4	180±2	5062
60	2000	641±16	208±8	141±1	353±8	167±4	5019
60	2500	629±8	195±8	139±2	340±6	167±3	4981
60	3000	612±1	195±7	132±2	334±6	159±3	4929
100	0	1130±0	244±0	172±0	539±0	254±0	5667
100	2000	971±13	253±11	153±1	492±8	217±3	5518
100	2500	923±12	272±10	151±2	489±8	206±3	5477
100	3000	863±7	259±10	145±1	460±7	195±2	5443
100	3500	856±13	273±11	137±3	467±9	186±4	5400
100	4000	838±16	280±10	140±3	466±8	185±4	5366
140	0	1434±0	299±0	179±0	677±0	291±0	6057
140	2000	1300±18	301±9	165±1	634±9	262±4	5927
140	2500	1257±17	320±7	162±1	632±7	252±3	5892
140	3000	1179±21	321±9	153±2	607±9	235±4	5861
140	3500	1141±16	336±9	153±2	605±8	228±3	5826
140	4000	1117±17	325±12	149±3	589±10	223±4	5787
low-spin state							
20	0	593±0	115±0	148±0	274±0	180±0	4760
20	1000	508±7	115±5	139±1	246±4	159±2	4638
20	1500	467±7	123±5	134±1	238±4	148±2	4583
20	2000	409±10	119±6	129±1	216±5	135±2	4508
20	2500	392±7	111±6	120±1	205±4	128±2	4438
20	3000	327±11	119±7	118±2	188±6	112±3	4374
60	0	943±0	163±0	160±0	423±0	231±0	5350
60	1000	842±7	174±4	151±1	397±4	209±2	5256
60	1500	808±15	167±9	150±1	381±8	204±3	5212
60	2000	782±20	187±9	146±1	385±9	196±4	5175
60	2500	740±10	182±10	141±2	368±8	186±3	5126
60	3000	668±12	200±8	138±1	356±6	171±3	5077
100	0	1274±0	209±0	167±0	564±0	272±0	5806
100	2000	1089±14	215±13	154±2	506±10	238±3	5661
100	2500	1062±20	241±12	154±1	515±10	231±4	5617
100	3000	950±21	261±9	154±2	491±9	214±4	5578
100	3500	906±19	255±11	146±2	472±10	203±4	5542
100	4000	866±18	260±12	144±2	462±10	195±4	5507
140	0	1593±0	253±0	171±0	699±0	307±0	6188
140	2000	1409±17	283±11	162±1	658±9	275±3	6061
140	2500	1308±24	319±12	160±1	649±11	256±5	6029
140	3000	1293±17	309±12	159±2	637±10	256±4	5996
140	3500	1293±17	307±12	159±2	636±10	256±4	5963
140	4000	1196±27	324±15	153±3	614±14	236±6	5927

Table S6. Calculated adiabatic elastic constants, bulk moduli, shear moduli and density, from molecular dynamics simulations. Note that, pressures exclude the +3.5 GPa pressure correction. Uncertainties are the standard error of the mean.

P (GPa)	*T* (K)	C_{11} (GPa)	C_{12} (GPa)	C_{44} (GPa)	*K* (GPa)	*G* (GPa)	*ρ* (kgm^{-3})
high-spin state							
20	0	505±0	136±0	145±0	259±0	160±0	4600
20	1000	432±5	146±4	132±0	242±3	136±1	4471
20	1500	411±7	150±5	127±1	237±4	128±2	4416
20	2000	358±10	151±5	123±1	220±5	115±2	4350
20	2500	351±11	153±5	114±1	219±5	108±2	4288
20	3000	314±9	147±8	110±2	203±6	99±3	4192
60	0	825±0	191±0	161±0	402±0	212±0	5201
60	1000	733±11	195±5	149±1	375±5	189±2	5116
60	1500	736±8	220±5	145±1	392±4	183±2	5062
60	2000	657±17	225±8	141±1	369±8	167±4	5019
60	2500	653±10	219±9	139±2	363±7	167±3	4981
60	3000	636±12	219±8	132±2	358±7	159±3	4929
100	0	1130±0	244±0	172±0	539±0	254±0	5667
100	2000	992±13	275±11	153±1	514±9	217±3	5518
100	2500	942±13	291±10	151±2	508±8	206±3	5477
100	3000	879±8	275±10	145±1	476±8	195±3	5443
100	3500	877±17	294±13	137±3	488±10	186±4	5400
100	4000	871±18	314±11	140±3	499±10	185±4	5366
140	0	1434±0	299±0	179±0	677±0	291±0	6057
140	2000	1317±19	318±10	165±1	651±9	262±4	5927
140	2500	1274±17	337±8	162±1	649±8	252±3	5892
140	3000	1207±22	348±10	153±2	635±10	235±5	5861
140	3500	1165±18	360±11	153±2	629±10	228±4	5826
140	4000	1145±19	353±14	149±3	617±11	223±5	5787
low-spin state							
20	0	593±0	115±0	148±0	274±0	180±0	4760
20	1000	516±7	123±5	139±1	254±4	159±2	4638
20	1500	479±7	135±5	134±1	250±4	148±2	4583
20	2000	426±11	135±7	129±1	232±6	135±3	4508
20	2500	412±9	131±7	120±1	224±5	128±2	4438
20	3000	347±12	139±8	118±7	208±7	112±5	4374
60	0	943±0	163±0	160±0	423±0	231±0	5350
60	1000	850±7	182±4	151±1	404±4	209±2	5256
60	1500	822±15	182±9	150±1	395±8	204±3	5212
60	2000	796±20	200±10	147±1	399±9	196±4	5175
60	2500	758±11	201±11	141±2	387±8	186±3	5126
60	3000	690±17	222±11	138±1	378±9	171±4	5077
100	0	1274±0	209±0	167±0	564±0	272±0	5806
100	2000	1107±14	233±14	154±2	524±10	238±4	5661
100	2500	1079±21	258±12	154±1	532±11	231±4	5617
100	3000	978±23	289±11	154±2	519±11	214±5	5578
100	3500	940±23	290±15	146±2	506±13	203±5	5542
100	4000	898±20	292±13	144±2	494±11	195±5	5507
140	0	1593±0	253±0	171±0	699±0	307±0	6188
140	2000	1419±17	293±11	162±1	669±9	275±4	6061
140	2500	1319±25	331±12	160±1	660±12	256±5	6029
140	3000	1313±19	330±13	159±2	657±11	255±4	5996
140	3500	1316±19	331±13	159±2	659±11	256±4	5963
140	4000	1224±31	352±18	153±3	643±16	236±7	5927

Supplemental reference list

Alfe, D. (2009). PHON: A program to calculate phonons using the small displacement method. Computer physics communications, 180(12), 2622-2633. https://doi.org/10.1016/j.cpc.2009.03.010

Cococcioni, M. & De Gironcoli, S. (2005). Linear response approach to the calculation of the effective interaction parameters in the LDA+U method. Physical review. B, Condensed matter and materials physics, 71(3), 035105.035101-035105.035116. https://doi.org/10.1103/PhysRevB.71.035105

Flyvbjerg, H. & Petersen, H. G. (1989). Error estimates on averages of correlated data. The Journal of Chemical Physics, 91(1), 461-466. https://doi.org/10.1063/1.457480

Kantor, I., Dubrovinsky, L., McCammon, C., Steinle-Neumann, G., Kantor, A., Skorodumova, N., et al. (2009). Short-range order and Fe clustering in Mg1-xFexO under high pressure. Physical Review B, 80(1), 014204. https://doi.org/10.1103/PhysRevB.80.014204

Lyubutin, I. S., Struzhkin, V. V., Mironovich, A. A., Gavriliuk, A. G., Naumov, P. G., Lin, J.-F., et al. (2013). Quantum critical point and spin fluctuations in lower-mantle ferropericlase. Proceedings of the National Academy of Sciences, 110(18), 7142. https://doi.org/10.1073/pnas.1304827110

Monkhorst, H. J. & Pack, J. D. (1976). Special points for Brillouin-zone integrations. Physical Review B, 13(12), 5188.

Speziale, S., Milner, A., Lee, V. E., Clark, S. M., Pasternak, M. P. & Jeanloz, R. (2005). Iron spin transition in Earth's mantle. Proceedings of the National Academy of Sciences, 102(50), 17918-17922.

Stackhouse, S. & Brodholt, J. P. (2007). The High-Temperature Elasticity of MgSiO3 Post-Perovskite. In K. Hirose, J. P. Brodholt, T. Lay and D. Yen (Eds.), Post-Perovskite : The Last Mantle Phase Transition (pp. 99-113). Washington: American Geophysical Union.

Wallace, D. C. (1972). Thermodynamics of Crystals. Mineola, NY: Dover Publications.